

# OCEAN-E2E: HYBRID PHYSICS-BASED AND DATA-DRIVEN GLOBAL FORECASTING OF MARINE HEATWAVES WITH END-TO-END NEURAL ASSIMILATION

**Anonymous authors**

Paper under double-blind review

## ABSTRACT

This work focuses on the end-to-end forecast of global extreme marine heatwaves (MHWs), which are unusually warm sea surface temperature events with profound impacts on marine ecosystems. Accurate prediction of extreme MHWs has significant scientific and financial worth. However, existing methods still have certain limitations in forecasting general patterns and extreme events. In this study, to address these issues, based on the physical nature of MHWs, we created a novel hybrid data-driven and numerical MHWs forecast framework Ocean-E2E, which is capable of 40-day accurate MHW forecasting with end-to-end data assimilation. Our framework significantly improves the forecast ability of MHWs by explicitly modeling the effect of oceanic mesoscale advection and air-sea interaction based on a dynamic kernel. Furthermore, Ocean-E2E is capable of end-to-end MHWs forecast and regional high-resolution prediction, allowing our framework to operate completely independently of numerical models while outperforming the current state-of-the-art ocean numerical/AI forecasting-assimilation models. Experimental results show that the proposed framework performs excellently on global-to-regional scales and short-to-long-term forecasts, especially in those most extreme MHWs. Overall, our model provides a framework for forecasting and understanding MHWs and other climate extremes.

## 1 INTRODUCTION

Marine heatwaves (MHWs) are abnormally warm seawater events that significantly damage marine ecosystems Oliver et al. (2021); Pearce et al. (2011). In other words, MHWs are extreme **Sea Surface Temperature Anomaly (SSTA)** events. MHWs, particularly extreme ones, can cause coral bleaching Hughes et al. (2017; 2018) and widespread mortality of marine organisms Garrabou et al. (2009); Thomson et al. (2015). As a result, precise forecasting of extreme MHWs has significant scientific and economic implications. For example, synoptic scale MHWs forecasting can help seafood production and management planning, such as feed cycles, at 1-7 day timescales, while subseasonal to seasonal forecasting can further support proactive decision-making for the blue economy Hobday et al. (2016); Malick et al. (2020); Mills et al. (2017); Payne et al. (2022). In this study, we will mainly focus on the subseasonal-to-seasonal forecast (i.e., 1-40 days).

Traditional MHW forecasting has primarily relied on two paradigms: physics-based numerical models and emerging data-driven approaches. Numerical models solve oceanic primitive equations to produce seasonal forecasts that capture large-scale patterns of MHW onset and intensification Jacox et al. (2022); Brodie et al. (2023), as well as sub-seasonal predictions that resolve finer-scale variability over shorter lead times Benthuisen et al. (2021); Yu et al. (2024). In parallel, recent advances in deep learning have shown promise for efficient global ocean forecasting Bi et al. (2022); Chen et al. (2023a); Kurth et al. (2023), with extensions to MHW prediction Lin et al. (2023); Sun et al. (2023). Despite their operational value, both paradigms suffer from inherent limitations:

1) **Numerical models:** These approaches demand substantial computational resources Xiong et al. (2023); Wang et al. (2024), especially in the data assimilation processes. Moreover, they often parameterize key physical processes—such as air-sea coupling and mesoscale eddy dynamics—through

empirical formulations, leading to systematic biases and constrained skill in predicting the general patterns of MHWs Jacox et al. (2022); Giamalaki et al. (2022).

2) **Data-driven models:** While these methods statistically approximate complex oceanic dynamics, they frequently generate non-physical fields, exhibiting limited accuracy in forecasting extreme events like MHWs due to issues such as error accumulation and smoothing of SST gradients during autoregressive rollouts Wang et al. (2024). Additionally, they typically depend on initialization from numerical models, precluding end-to-end operation from raw observational inputs Xiong et al. (2023).

Given these complementary strengths and weaknesses, a natural question arises: *why not integrate the advantages of both by combining a relatively simple physical model with AI components, where the physical model handles well-understood dynamics and AI simulates the more complex or uncertain aspects?* In this study, we pursue this hybrid strategy to effectively mitigate the aforementioned drawbacks of numerical and data-driven models, enabling our framework to harness the best of both worlds:

1) **Enhanced computational efficiency and end-to-end capability:** By substituting neural networks for the forecasting and data assimilation processes, we have substantially reduced the cost of predicting MHWs, enabling our framework to operate independently of numerical models.

2) **Improved physical realism and reduced biases:** The incorporation of physical constraints ensures generation of consistent fields, addressing the non-physical artifacts and extreme-event limitations in pure data-driven methods.

By addressing these integrated shortcomings, we introduce Ocean-E2E, a global hybrid physics-based data-driven framework that significantly enhances forecasts of extreme MHWs, drawing inspiration from numerical models. The contributions of this paper can be summarized as follows: (1) **Global/Regional MHWs Forecasting Framework.** We propose a hybrid physics-based data-driven method that supports both global scale and regional high-resolution forecasting, achieving high-accuracy results for extreme MHWs forecasts. (2) **Global MHWs Neural Assimilation Framework.** We designed an end-to-end MHWs neural system that, when combined with the forecasting model, can directly obtain the complete initial field and forecasting results of MHWs from observation data. (3) **Physics-consistent Forecast.** By combining physical laws into our framework, our model has achieved state-of-the-art results in long-term and regional high-resolution forecasting with higher physical consistency.

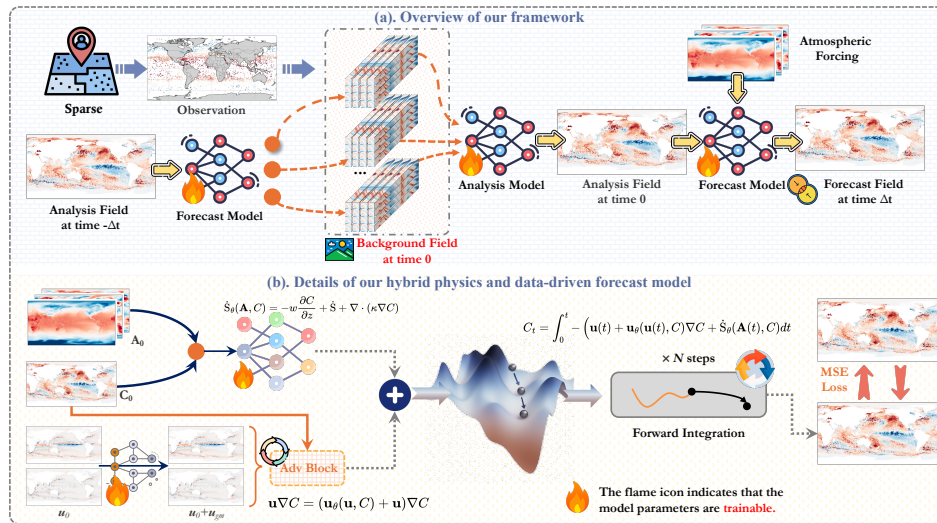


Figure 1: Our proposed Ocean-E2E framework. a) Overview of our framework. b) Details of our hybrid physics and data-driven forecast model.

## 2 METHOD

### 2.1 FRAMEWORK OVERVIEW

In this study, the problem of the end-to-end MHWs forecast is **essentially forecasting SSTA**, which can be separated into two parts (shown in Figure 1). First, estimating the current state of SSTA  $C_0 \in \mathbb{R}^{H \times W}$  (a global two-dimensional field, where  $H$  and  $W$  correspond to latitude and longitude) based on the observation  $C_0^{obs}$  and the background field  $C_0^{bg}$ . Second, predicting the future state of mixed layer SSTA  $C_t$  based on the current state  $C_0$  under atmospheric forcing  $A_{0:t} \in \mathbb{R}^{C \times H \times W}$ . Here  $A_{0:t}$  denotes the atmosphere state from time 0 to  $t$ . Formally speaking, we are going to model the conditional distribution  $p(C_t | C_0^{obs}, C_0^{bg}, A_{0:t}, \cdot)$  in two stages:

$$p(C_t | C_0^{obs}, C_0^{bg}, A_{0:t}) = \underbrace{p^f(C_t | C_0, A_{0:t})}_{\text{Forecast model}} \cdot \underbrace{p^a(C_0 | C_0^{obs}, C_0^{bg})}_{\text{Assimilation model}} \quad (1)$$

where  $p^f$  and  $p^a$  denote forecast and assimilation process, respectively. In our end-to-end framework, we model these two processes through two specifically designed neural networks  $\phi_\theta^f$  and  $\phi_\theta^a$ , which we will discuss in detail in the following sections.

### 2.2 THE DESIGN OF $\phi_\theta^f$ : HYBRID PHYSICS-AI MODEL

As established in the problem formulation, forecasting MHWs fundamentally reduces to predicting extreme sea surface temperature anomalies (SSTA). To effectively embed physical principles into our modeling framework, we must rigorously account for the governing laws of SSTA evolution. We approach this challenge through a generalized geophysical fluid dynamics perspective, wherein seawater temperature constitutes a *passive tracer* advected by oceanic flow fields. Formally speaking, the governing equation of SSTA  $C$ , together with other surface variables can be written as:

$$\frac{\partial C}{\partial t} + (\mathbf{u}_g + \mathbf{u}_{ag}) \nabla C + w \frac{\partial C}{\partial z} = \dot{S} \quad (2)$$

$$f \mathbf{k} \times \mathbf{u}_g = -\nabla(g\eta) \quad (3)$$

$$\frac{\partial \eta}{\partial t} + \nabla \cdot (H \hat{\mathbf{u}}) = 0 \quad (4)$$

$$\frac{\partial \hat{\mathbf{u}}}{\partial t} + \widehat{\mathbf{G}}_u + \nabla(g\eta) = 0 \quad (5)$$

$$w|_{z=0} = \eta_t \quad (6)$$

Where  $t$  is time,  $(\mathbf{u}, w) = (\mathbf{u}_g + \mathbf{u}_{ag}, w)$  are horizontal and vertical flow velocity ( $\mathbf{u}_g$  represents oceanic geostrophic velocity while  $\mathbf{u}_{ag}$  is ageostrophic velocity),  $\nabla$  is the horizontal derivation,  $\dot{S}$  is the sink/source,  $\mathbf{k}$  is a unit vector in the vertical direction,  $f$  is the Coriolis parameter,  $\eta$  is sea surface height,  $H$  is ocean depth,  $\hat{\cdot}$  is vertical average operator (i.e.,  $\hat{\mathbf{u}} = \int_{-H}^0 \mathbf{u} dz$ ),  $g$  is the gravitational acceleration. By integrating equation (1), the state of  $C$  at time  $t$  can be expressed in the form of the initial condition  $C_0$ :

$$\begin{aligned} C_t &= \int_0^t -\mathbf{u}_g \nabla C + (-\mathbf{u}_{ag} \nabla C - w \frac{\partial C}{\partial z} + \dot{S}) dt + C_0 \\ &\simeq \int_0^t \underbrace{-\mathbf{u}_g \nabla C}_{\text{advective transport}} + \underbrace{(-\mathbf{u}_{ag} \nabla C + \dot{S})}_{\text{mixing and external sink/source}} dt + C_0 \end{aligned} \quad (7)$$

The second equal sign is due to the fact that, according to equation (5),  $w|_{z=0}$  is small ( $10^{-6} \sim 10^{-5}$  m/s) compared to other terms. Equation (7) implies two key governing mechanisms of MHWs: 1) **advective transport** by geostrophic currents that redistribute thermal energy, 2) **mixing and external sink/source** encompassing convective mixing and external ageostrophic forcing through surface boundary interactions. In the following paragraphs, we will combine physical theory and deep learning methods to simulate these two mechanisms in four steps.

**Step 1. Modelling advective transport.** The key factor of advective transport is the ocean surface current  $\mathbf{u}_g$ , where the flow field at the smaller scale (mesoscale) plays an important role in the distribution of MHWs and other oceanic passive tracers. However, in most models and data, due to limited resolution, the model cannot distinguish these small-scale processes, so the advection processes caused by the flow field below the model’s finest grid (i.e., subgrid processes):

$$\overline{\mathbf{u}_g \nabla C} = \overline{\mathbf{u}_g} \nabla \overline{C} + \overline{\mathbf{u}'_g \nabla C'} \quad (8)$$

are not fully simulated. Here, the overline  $\overline{\cdot}$  represents the downsampling operator. In other words, the variables with an overline denote the low-resolution data. In the traditional numerical model, Gent and McWilliams Gent & McWilliams (1990) found that this subgrid process can be fitted by ‘bolus velocity’ (also called GM90 parameterization):

$$\overline{\mathbf{u}'_g \nabla C'} \sim \mathbf{u}_{gm} \nabla \overline{C} \quad (9)$$

According to the GM90 parameterization, these bolus velocity can be expressed as Gent & McWilliams (1990):

$$\mathbf{u}_{gm} = (\kappa \nabla \rho / \rho_z)_z \quad (10)$$

where  $\rho = \rho(C)$  is the density. It should be noticed that this expression requires subsurface ocean data, which is often extremely difficult to obtain. What’s more, the choice of coefficient  $\kappa$  requires an empirical formula, which is always inaccurate. Alternatively, we seek a neural network  $\mathbf{u}_\theta(\mathbf{u}_g, C) = \mathbf{u}_{gm}$  to approximate the bolus velocity and the subgrid advection effect. In summary, the advection term can be expressed as:

$$\mathbf{u}_g \nabla C = (\mathbf{u}_\theta(\mathbf{u}_g, C) + \mathbf{u}_g) \nabla C \quad (11)$$

**Step 2. Modelling mixing and external sink/source.** This term is strongly related to the air-sea interaction along the ocean’s surface. To be specific, for SSTA, the source term consists of four parts:

$$\dot{S} \propto Q'_{\text{net}} = Q'_{\text{SW}} + Q'_{\text{LW}} + Q'_{\text{sh}} + Q'_{\text{lh}} \quad (12)$$

where  $Q_{\text{SW}}, Q_{\text{LW}}, Q_{\text{sh}}, Q_{\text{lh}}$  are the shortwave radiation, longwave thermal radiation, sensible heat flux, and latent heat flux, respectively. Of the four air-sea heat fluxes, the sensible and latent flux  $Q'_{\text{sh}} + Q'_{\text{lh}}$  determines the majority of the SSTA’s variations Holbrook et al. (2019). According to the bulk formula Cui et al. (2025), these two terms are significantly related to surface wind speed  $U_{10}, V_{10}$ , near-surface temperature of the atmosphere  $T_{2m}$ , and surface specific humidity  $q_a$ . What’s more, the ageostrophic velocity  $\mathbf{u}_{ag}$  is also driven by surface wind forcing  $U_{10}, V_{10}$ . Based on the observation above, we assume that mixing and external sink/source can be well approximated by the surface variables of the atmosphere  $\mathbf{A} = (U_{10}, V_{10}, T_{2m}, q_a)$  and  $C$  itself. Specifically,

$$\dot{S}_\theta(\mathbf{A}, C) = -\mathbf{u}_{ag} \nabla C + \dot{S} \quad (13)$$

Since this study primarily focuses on proposing a physics-AI **framework**, the design and selection of the specific structures for the two neural networks  $\mathbf{u}_\theta, \dot{S}_\theta$  are highly flexible. In this study, we selected a powerful and robust spatiotemporal prediction backbone Tan et al. (2022) to accomplish this task. We believe that more advanced backbones can further enhance the model’s prediction performance.

**Step 3. Treating boundary conditions.** Above paragraphs point out that in order to effectively model the key physical mechanism of MHWs, we need the future state of  $\mathbf{A}$  and  $\mathbf{u}_g$  (i.e., boundary conditions). For oceanic geostrophic velocity  $\mathbf{u}_g, \frac{\partial}{\partial t}(3) - \nabla \cdot (H(4))$  implies that

$$\frac{\partial^2 \eta}{\partial t^2} + \nabla \cdot (gH \nabla \eta) = \nabla \cdot \widehat{\mathbf{G}}_u \simeq \nabla \cdot \widehat{\mathbf{G}}_{u_g} \triangleq \mathcal{G}(\eta) \quad (14)$$

which is a self-consistent hyperbolic equation. This indicates that, at least at a relatively short time interval, the evolution of  $\eta$ , together with geostrophic velocity, can be modelled based on an auto-regressive manner:

$$\frac{\partial \mathbf{u}_g}{\partial t} = \mathcal{M}_\theta(\mathbf{u}_g) \quad (15)$$

Here  $\mathcal{M}_\theta$  is a pretrained neural network. Inspired by the Wu et al. (2024b) architecture, the neural network module  $\mathcal{M}_\theta$  used for modeling ocean surface geostrophic velocity employs a U-Net-like encoder-decoder structure. This model is primarily built upon the **Group Attention Block**

(**GABlock**), which serves as the core computational unit. The **GABlock** is designed to efficiently capture multi-scale spatio-temporal features, leveraging a **Spatial Attention (SA)** module that incorporates depth-wise and depth-wise dilated convolutions for spatial gating, followed by a **Multilayer Perceptron (MLP)**. The overall architecture processes initial geostrophic current conditions, uses downsampling and stacked **GABlocks** in the encoder to extract features, and then symmetrically reconstructs the resolution in the decoder via upsampling and skip connections to predict the future geostrophic velocity field. What’s more, the atmosphere variables between time interval  $[0, t]$  is also acquired through a large AI-driven weather forecast model Gao et al. (2025):

$$\frac{\partial \mathbf{A}}{\partial t} = \mathcal{N}_\theta(\mathbf{A}) \quad (16)$$

**Step 4. Combining physics and AI together.** As shown in the section above, the future state of  $C$  at time  $t$  can be modelled as:

$$C_t = \int_0^t - \left[ \int_0^s \mathcal{M}_\theta(\mathbf{u}_g) ds + \mathbf{u}_\theta \left( \int_0^s \mathcal{M}_\theta(\mathbf{u}_g) ds, C \right) \right] \nabla C + \dot{S}_\theta \left( \int_0^s \mathcal{N}_\theta(\mathbf{A}) ds, C \right) ds \quad (17)$$

In the training stage, we first pretrain these two neural networks  $\mathcal{M}_\theta, \mathcal{N}_\theta$ . Then the parameters of these networks are frozen and we utilize the forecast model to optimize the parameters of  $\mathbf{u}_\theta, \dot{S}_\theta$  based on the MSE loss, which can be written as:

$$\mathcal{L} = \|\hat{C}_t - \int_0^t -(\mathbf{u}_g + \mathbf{u}_\theta(\mathbf{u}_g, C)) \nabla C + \dot{S}_\theta(\mathbf{A}, C) dt\|^2 \quad (18)$$

Where  $\hat{C}_t$  is the groundtruth data of  $C_t$ . In practice, by separating the time interval  $[0, t]$  into  $N$  subintervals  $[i\Delta t, (i+1)\Delta t], 1 \leq i \leq N-1$ , equation (18) is approximated via forward Euler method:

$$C_{(i+1)\Delta t} = C_{i\Delta t} + \left[ -(\mathbf{u}_{i\Delta t} + \mathbf{u}_\theta(\mathbf{u}_{i\Delta t}, C_{i\Delta t})) \nabla C_{i\Delta t} + \dot{S}_\theta(\mathbf{A}_{i\Delta t}, \mathbf{A}_{(i+1)\Delta t}, C_{i\Delta t}) \right] \Delta t, \quad (19)$$

$$\mathbf{u}_{(i+1)\Delta t} = \mathbf{u}_{i\Delta t} + \mathcal{M}_\theta(\mathbf{u}_{i\Delta t}) \Delta t, \quad (20)$$

$$\mathbf{A}_{(i+1)\Delta t} = \mathbf{A}_{i\Delta t} + \mathcal{N}_\theta(\mathbf{A}_{i\Delta t}) \Delta t. \quad (21)$$

Then the parameters of  $\mathbf{u}_\theta, \dot{S}_\theta$  are optimized through  $\mathcal{L} = \|\hat{C}_t - C_{N\Delta t}(\theta)\|^2$ . It is worth noting that the above numerical kernel is highly **lightweight**, imposing no significant computational burden on our framework. Details of the numerical implementation can be found in Appendix C.

### 2.3 THE DESIGN OF $\phi_\theta^g$ : NEURAL DATA ASSIMILATION

As shown in the above section, our hybrid AI-physics model requires an initial condition  $C_0$  to initialize our framework. However, under realistic operational forecasting scenarios, the full  $C_0$  (analysis field) cannot be directly observed. This necessitates a data assimilation (DA) process that optimally combines sparse observational data  $C_0^{obs}$  with prior background estimates  $C_0^{bg}$  from numerical models, which requires large computational resources Boudier et al. (2023).

Our framework addresses these limitations by establishing a **direct mapping** from observational inputs  $C_0^{obs}$  to assimilated states  $C_0$  through deep learning. We utilized neural networks to optimally combine sparse observations with background fields in one step. Specifically, we begin with the SSTA state at time  $-\Delta t$  ( $C_{-\Delta t}$ ), defining  $[-\Delta t, 0]$  as the assimilation window. We generate background fields ( $C_0^{bg}$ ) by adding structured noise to  $C_{-\Delta t}$ :

$$C_0^{bg} = \phi_\theta^f(C_{-\Delta t} + \varepsilon, \mathbf{A}_{0:\Delta t}) \quad (22)$$

where  $\varepsilon$  denotes Perlin noise. The final analysis field is then produced by merging observations with background data:

$$C_0 = \phi_{\theta}^a(C_0^{obs}, C_0^{bg}) \quad (23)$$

where  $\phi_{\theta}^a$  is an edge-reparameterization and attention-guided network with Kirsch-guided reparameterization, which is capable of reconstructing SSTA fields from sparse observations Liu et al. (2024). The neural assimilation network  $\phi_{\theta}^a$ , inspired by Liu et al. (2024), is an edge-reparameterization and attention-guided architecture meticulously designed for the efficient, real-time projection of observation data to analysis data. The network’s core innovation lies in its Kirsch-guided Reparameterization Module (KRM), which efficiently consolidates standard, expanded, and eight directional Kirsch edge-detection convolutions into a single unit during inference, enabling robust capture of sharp feature boundaries. Complementing this, the network employs a joint Channel and Spatial Attention mechanism (CAM and SAM) to dynamically focus computational resources on crucial data regions. The final architecture is a cascaded, iterative structure built upon a Basic Block that includes the attention modules, where the observation data is passed through five consecutive stages, each integrating the KRM output with a residual connection to progressively refine the analysis and produce the highly accurate, edge-aware output. The details of  $\phi_{\theta}^a$  can be found in Appendix D.

Once the initial analysis field  $C_0$  is obtained, the model proceeds with forward assimilation over subsequent time steps to maintain accuracy in evolving forecasts. Starting from  $C_0$ , the framework iteratively advances the state by generating a background estimate for the next time step  $C_{\Delta t}^{bg}$  using the forward operator and incorporating dynamical updates at a time interval  $\Delta t$  (i.e., assimilation window). For instance, at  $i$ -th time step, the background is computed as:

$$C_{(i+1)\Delta t}^{bg} = \phi_{\theta}^f(C_{i\Delta t} + \varepsilon_i, A_{i\Delta t:(i+1)\Delta t}) \quad (24)$$

followed by the assimilation step:

$$C_{(i+1)\Delta t} = \phi_{\theta}^a(C_{(i+1)\Delta t}^{obs}, C_{(i+1)\Delta t}^{bg}) \quad (25)$$

As we will demonstrate in the following paragraph, this autoregressive process can generate robust assimilation fields over hundreds of days.

### 3 EXPERIMENTS

We designed comprehensive experiments to evaluate our model. Our evaluation is guided by the following key questions: **RQ1: Overall Performance:** Can Ocean-E2E outperform state-of-the-art models with higher consistency and better performance in normal and extreme MHW events? **RQ2: End-to-end Forecasting:** Can Ocean-E2E run independently of numerical model while preserving a high accuracy in real-world MHWs forecast? **RQ3: High-resolution Multiscale Prediction:** Can our framework achieve a satisfying performance in regional high-resolution simulations, where complicated oceanic multi-scale dynamics pose more challenges to the model’s forecast skill and physical consistency?

#### 3.1 BENCHMARKS AND BASELINES

We conduct the experiments on GLORYS12V1 reanalysis data Lellouche et al. (2018), which provides daily mean data of sea surface temperature (SST) covering latitudes between  $-80^\circ$  and  $90^\circ$  spanning between 1993 and 2021. The seasonal cycle has been removed from the original data in order to get the MHWs (SSTA) field Shu et al. (2025). The subset we use includes years from 1993 to 2021, which is 1993-2018 for training, 2019 for validating, and 2020-2021 for testing. The surface velocity of the ocean is obtained from satellite observation Pujol et al. (2016). The atmospheric variables are obtained from ECWMF Reanalysis v5 (ERA5) Hersbach et al. (2020). More details, including observational data and atmospheric forcing data, can be found in Appendix B.

Before introducing our experiments, there are two key concepts that should be clarified: **ocean simulation** and **end-to-end ocean forecast**. As pointed out in previous studies Shu et al. (2025);

Table 1: In the global ocean simulation task, we compare the performance of our Ocean-E2E with various baselines. The average results for global SSTA (Sea Surface Temperature Anomaly) are measured using RMSE and CSI. Lower RMSE ( $\downarrow$ ) and higher CSI ( $\uparrow$ ) indicate better performance. The best results are in **bold**, and the second-best are underlined. Note that some baseline models are unstable and produce unrealistic forecasts, with RMSE exceeding 10 K replaced by —.

Model Category	Metric							
	20-day		40-day		50-day		60-day	
	RMSE	CSI	RMSE	CSI	RMSE	CSI	RMSE	CSI
<b>Ocean Forecasting Models</b>								
🌩️ FourCastNet Pathak et al. (2022)	0.6836	0.2709	—	0.1755	—	0.1537	—	0.1423
🌩️ CirT Liu et al. (2025)	1.3496	0.0905	1.9249	0.0810	1.9932	0.0770	2.0321	0.0746
🌩️ WenHai Cui et al. (2025)	<b>0.5435</b>	<b>0.4202</b>	<b>0.7006</b>	<b>0.2805</b>	<b>0.7633</b>	<b>0.2447</b>	<b>0.8139</b>	<b>0.2209</b>
🌩️ ClimODE Verma et al. (2024)	0.7221	0.3263	0.8555	0.2091	0.8997	0.1896	—	0.1754
<b>Operator Learning Models</b>								
🧩 CNO Raonic et al. (2023)	0.7062	0.3669	0.9025	0.2367	0.9821	0.2011	1.0556	0.1771
🧩 LSM Wu et al. (2023)	1.1346	0.3025	—	0.1760	—	0.1436	—	0.1312
<b>Computer Vision Backbones</b>								
📷 U-Net Ronneberger et al. (2015)	0.6923	0.3909	0.8893	0.2629	0.9706	0.2292	1.0463	0.2054
📷 ResNet He et al. (2016)	—	0.2537	—	0.1538	—	0.1248	—	0.1029
📷 DiT Peebles & Xie (2023)	0.9390	0.3411	1.7051	0.2528	2.2474	0.2311	2.9139	0.2137
<b>Spatiotemporal Models</b>								
🏠 ConvLSTM Shi et al. (2015)	0.7135	0.3585	0.8920	0.2292	0.9726	0.1957	1.0545	0.1735
🏠 SimVP Tan et al. (2022)	0.6729	0.3749	0.8345	0.2736	0.8864	0.2413	0.9296	0.2162
🏠 PastNet Wu et al. (2024b)	1.3876	0.1867	1.4230	0.1760	1.4287	0.1733	1.4353	0.1705
🏆 <b>Ocean-E2E</b>	<b>0.5659</b>	<b>0.4285</b>	<b>0.6596</b>	<b>0.3230</b>	<b>0.6911</b>	<b>0.2874</b>	<b>0.7194</b>	<b>0.2580</b>
Promotion	—	2.0%	5.8%	15.1%	9.5%	17.4%	11.6%	16.8%

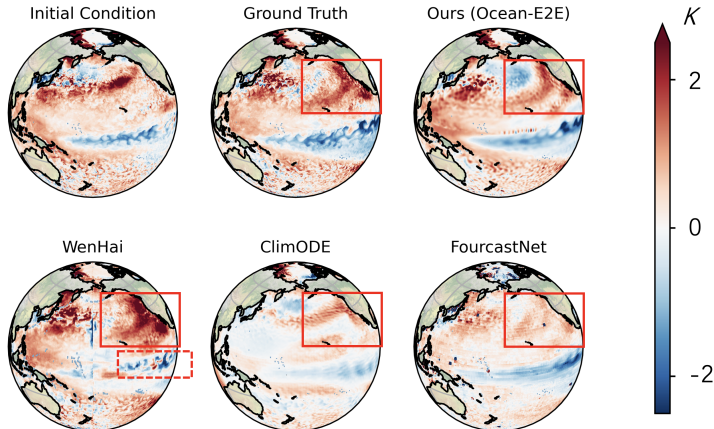


Figure 2: Snapshots of our framework and other baseline simulations at 60-day lead time. The simulations are initialized on August 7th, 2020. Red solid boxes represent MHW events while red dashed box indicates physical inconsistency in forecasting results.

Cui et al. (2025), the ocean simulation utilizes the current state of SSTA  $C_0$  to forecast future state  $C_t$  under the realistic atmosphere forcing  $\mathbf{A}_{0:t}$ . In contrast, the end-to-end forecast task includes assimilating the initial analysis field of SSTA  $C_0$  and forecasting only based on the current atmosphere state  $\mathbf{A}_0$ .

We compare the simulation performance of Ocean-E2E with 4 main categories of data-driven models: **ocean forecasting models** (Fourcastnet Kurth et al. (2023), CirT Liu et al. (2025), Wenhai Cui et al. (2025) and ClimODE Verma et al. (2024)), **operator learning models** (FNO Li et al. (2021), CNO

Table 2: In operational global ocean forecast task, we compare the performance of our Ocean-E2E with S2S. The average results for global SSTA of RMSE are recorded for 2020 and 2021. A small RMSE ( $\downarrow$ ) indicates better performance. The best results are in **bold**.

MODEL	METRIC (RMSE)							
	2020				2021			
	10-DAY	20-DAY	30-DAY	40-DAY	10-DAY	20-DAY	30-DAY	40-DAY
S2S	0.8140	0.8870	0.9514	0.9965	0.8261	0.8897	0.9450	0.9895
OCEAN-E2E (OURS)	<b>0.5750</b>	<b>0.6047</b>	<b>0.7514</b>	<b>0.8747</b>	<b>0.6414</b>	<b>0.7447</b>	<b>0.8147</b>	<b>0.8729</b>
OCEAN-E2E (PROMOTION)	29.4%	31.8%	21.02%	12.2%	22.4%	16.3%	13.7%	11.7%

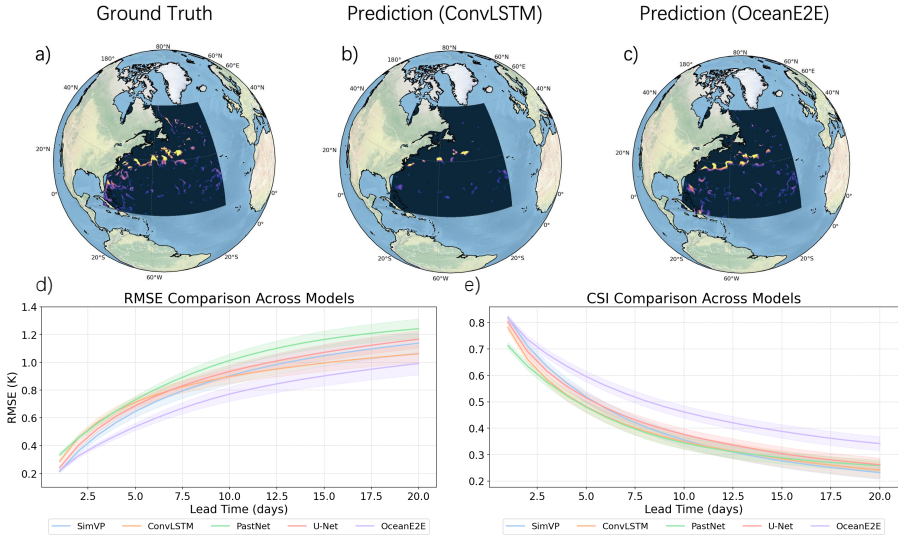


Figure 3: Results of our regional high resolution MHWs simulation in western Atlantic Ocean. a)-c) Snapshots of our simulation, where **yellow** parts indicate MHWs. d)-e) RMSE and CSI of our Ocean-E2E and other baselines.

Raonic et al. (2023) and LSM Wu et al. (2023)), **computer vision backbones** (U-Net Ronneberger et al. (2015), ResNet He et al. (2016) and DiT Peebles & Xie (2023)) and **spatiotemporal models** (ConvLSTM Shi et al. (2015), SimVP Tan et al. (2022) and PastNet Wu et al. (2024b)).

We also compare the end-to-end operational forecast ability against **traditional numerical operational forecast system**: ECWMF sub-seasonal to seasonal prediction (S2S). S2S is currently the superior subseasonal-to-seasonal weather forecast model that provides the forecast of atmosphere and ocean surface physics at a lead time of 40 days. The original resolution is  $1.5^\circ$ , and we upsample the data to  $1/2^\circ$  for comparison.

### 3.2 EVALUATION METRIC

We utilized two metrics, RMSE (Root Mean Square Error) and CSI (Critical Success Index), to evaluate the forecast performance. The RMSE represents the **overall performance** of our framework’s forecast, while CSI mainly focuses on the most **extreme MHW events**. What’s more, we utilize assimilation bias (BIAS) to assess the systematic bias induced by our neural assimilation system. More details can be found in Appendix E.

### 3.3 EVALUATION OF OCEAN SIMULATION PERFORMANCE (RQ1)

As shown in Table 1, it can be found that in long-term ocean simulations (40-60 days), our framework performs better compared to the baseline. On day 60, the RMSE decreased by an average of 11.6%

and the CSI increased by an average of 9.2%. In shorter simulations (20 days), our model was slightly lower than WenHai but significantly higher than other baselines. This indicates that our Ocean-E2E can capture both general patterns and extreme events of MHWs. To further illustrate our simulation ability, we select a snapshot of our 60 days simulation, as shown in Figure 2. It can be found that a strong MHW is growing in the West Pacific Ocean (red solid box in Figure 2). Compared to other baselines, our Ocean-E2E shows a robust forecast result and better consistency with ground truth.

### 3.4 EVALUATION OF THE END-TO-END NEURAL ASSIMILATION AND FORECAST PERFORMANCE (RQ2)

We conducted two sets of assimilation experiments using analysis fields from January 1, 2020 and January 1, 2021 as initial conditions, respectively. Both experiments employed a 6-day assimilation window to assimilate SSTA fields over a full year. As shown in Appendix G.1 (Figure 5), the RMSE and BIAS evolution reveal that assimilation errors rapidly increase and stabilize during the assimilation process, demonstrating the stability of our assimilation framework.

Using these assimilated fields as initial conditions and GLORYS12V1 reanalysis as ground truth, we evaluate the forecasting performance of Ocean-E2E against the S2S system. **Since S2S provides 46 days of forecast data, in this study, we only compare the 10-40 days’ forecast results of Ocean-E2E with it.** To ensure experimental fairness, results in Table 2 were calculated after the assimilation outputs stabilized (12 days post-initialization). It can be found that Ocean-E2E achieves an average 10% reduction in RMSE compared to superior end-to-end numerical prediction systems across 40-day subseasonal-to-seasonal forecasts. Additional comparative experiments have been conducted using S2S assimilation fields as both reference truth and initial conditions (see Appendix G). In all experimental configurations, Ocean-E2E demonstrates superior performance relative to S2S, confirming its robust competitiveness.

### 3.5 REGIONAL HIGH-RESOLUTION SIMULATION (RQ3)

As discussed in Section 2.1, our framework builds upon the GM90 theoretical framework, which is also applicable to high-resolution data. To validate its performance, we implement a regional high-resolution simulation ( $1/12^\circ$ ) of the western Atlantic Ocean. Figure 3 a)-c) illustrate a comparison between Ocean-E2E and baselines. Compared to the ground truth, our model has more physical details with more extreme MHW events (yellow parts). Evaluation based on RMSE and CSI (Figure 3 d)-e)) also confirmed that Ocean-E2E achieves a state-of-the-art performance in regional simulations. **Furthermore, to verify physical consistency, we calculated the power spectrum of the Ocean-E2E simulation results and compared it with the baselines (see Appendix G.2). The results demonstrate that our model exhibits higher consistency with the real physical fields at small scales (high frequencies).**

Table 3: CSI of our ablation studies on model design, forcings, and neural architecture. The best results are in **bold**.

Variants	Global Simulation		Regional Simulation	
	20 day	60 day	10 day	30 day
<i>Physical Model Design</i>				
$\dot{S}_\theta$ (S only)	0.3884	0.1658	0.3913	0.1877
$(\mathbf{u}_\theta + \mathbf{u}_g)\nabla C$ (ADV only)	0.3207	0.1504	0.3207	0.0963
$\mathbf{u}_g\nabla C$ (pure numerical)	—	—	—	—
<i>Time-Varying Forcings</i>				
Static Atmosphere ( $\mathbf{A}(t) \leftarrow \mathbf{A}(0)$ )	0.2652	0.1223	0.3021	0.1470
Static Background Flow ( $\mathbf{u}_g(t) \leftarrow \mathbf{u}_g(0)$ )	0.3988	0.2115	0.4080	0.2245
<i>Neural Architecture Analysis</i>				
w/o GABlock (in $\mathcal{M}_\theta$ )	0.4015	0.2245	0.4322	0.2588
w/o MidXnet (in $\dot{S}_\theta, \mathbf{u}_\theta$ )	0.3540	0.1810	0.3890	0.2015
$(\mathbf{u}_\theta + \mathbf{u}_g)\nabla C + \dot{S}_\theta$ (Ours)	<b>0.4285</b>	<b>0.2580</b>	<b>0.4615</b>	<b>0.2926</b>

### 3.6 ABLATION STUDIES

To validate the effectiveness of the proposed framework, we perform an ablation analysis by sequentially removing core components in our global and regional simulation task. Since our main contribution is the framework rather than neural network design, we choose the two key components of our framework: the advection term  $(\mathbf{u}_\theta(\mathbf{u}_g, C) + \mathbf{u}_g)\nabla C$  (denoted as ADV) and the source term  $\dot{S}_\theta(\mathbf{A}, C)$  (denoted as S). As demonstrated in Table 3, the Critical Success Index (CSI) exhibits a marked reduction when either component is omitted, confirming their essential roles in enhancing simulation accuracy, particularly for extreme marine heatwaves (MHWs). Notably, the source term contributes most significantly to forecasting performance, underscoring the critical influence of air-sea interaction dynamics on MHW evolution. Moreover, if the neural networks are removed from the model (i.e., a pure numerical model), the model collapses quickly due to the numerical instability caused by large horizontal gradients in the advection terms. This stresses the importance of the GM ‘bolus’ velocity, which acts as a subgrid ‘damping’ term.

Furthermore, we investigated the impact of time-varying forcings by fixing the atmospheric forcing ( $\mathbf{A}$ ) and background flow ( $\mathbf{u}_g$ ) to their initial states. As shown in the second section of Table 3, using static atmospheric forcing results in a significant performance drop (e.g., Global 60-day CSI decreases to 0.1223), confirming that dynamic heat flux is critical for SSTA prediction. Similarly, fixing the background flow degrades performance, indicating the necessity of capturing the time-varying nature of large-scale ocean circulation.

Finally, we analyzed the contribution of specific neural network components. We examined the Group Attention Block (GABlock) in the background modeling branch and the MidXnet in the dynamical evolution branch. The results in the third section of Table 3 indicate that removing the GABlock leads to a noticeable decline in accuracy, verifying its importance in encoding background physics. Moreover, removing the MidXnet causes a substantial drop in performance, validating its critical role in capturing complex spatiotemporal dynamics in the latent space.

## 4 CONCLUSIONS

In this study, we introduce Ocean-E2E, a hybrid framework merging data-driven and numerical methods for end-to-end marine heatwave (MHW) forecasting. By resolving mesoscale advection and air-sea interactions with a dynamic kernel, it delivers stable 40-day global-to-regional MHW predictions in both simulation and forecast tasks. Neural assimilation enables independent high-resolution forecasting with enhanced accuracy and stability, via rapid error stabilization. Results confirm its robustness across scales, advancing MHW prediction and climate insights.

540 ETHICS STATEMENT

541

542 This work presents a framework for simulating ocean dynamics and does not raise any ethics concerns.

543

544

545 REPRODUCIBILITY STATEMENT

546

547 To guarantee the reproducibility of our results, the complete source code and data associ-  
548 ated with this study have been made publicly available. The implementation, which com-  
549 prises the simulation framework, training procedures, and evaluation scripts, can be accessed  
550 via the following anonymous GitHub link: [https://anonymous.4open.science/r/  
551 Ocean-E2E-anonymous-5994](https://anonymous.4open.science/r/Ocean-E2E-anonymous-5994).

552

553 REFERENCES

554

555 Rossella Arcucci, Jiangcheng Zhu, Shuang Hu, and Yi-Ke Guo. Deep data assimilation: integrating  
556 deep learning with data assimilation. *Applied Sciences*, 11(3):1114, 2021.

557

558 Jessica A Benthuisen, Grant A Smith, Claire M Spillman, and Craig R Steinberg. Subseasonal  
559 prediction of the 2020 great barrier reef and coral sea marine heatwave. *Environmental Research  
Letters*, 16(12):124050, 2021.

560

561 Kaifeng Bi, Lingxi Xie, Hengheng Zhang, Xin Chen, Xiaotao Gu, and Qi Tian. Pangu-weather:  
562 A 3d high-resolution model for fast and accurate global weather forecast. *arXiv preprint  
arXiv:2211.02556*, 2022.

563

564 Kaifeng Bi, Lingxi Xie, Hengheng Zhang, Xin Chen, Xiaotao Gu, and Qi Tian. Accurate medium-  
565 range global weather forecasting with 3d neural networks. *Nature*, 619(7970):533–538, 2023.

566

567 Pierre Boudier, Anthony Fillion, Serge Gratton, Selime Gürol, and Sixin Zhang. Data assimilation  
568 networks. *Journal of Advances in Modeling Earth Systems*, 15(4):e2022MS003353, 2023.

569

570 Julien Brajard, Alberto Carrassi, Marc Bocquet, and Laurent Bertino. Combining data assimilation  
571 and machine learning to emulate a dynamical model from sparse and noisy observations: A case  
study with the lorenz 96 model. *Journal of computational science*, 44:101171, 2020.

572

573 Stephanie Brodie, Mercedes Pozo Buil, Heather Welch, Steven J Bograd, Elliott L Hazen, Jarrod A  
574 Santora, Rachel Seary, Isaac D Schroeder, and Michael G Jacox. Ecological forecasts for marine  
resource management during climate extremes. *Nature Communications*, 14(1):7701, 2023.

575

576 Kang Chen, Tao Han, Junchao Gong, Lei Bai, Fenghua Ling, Jing-Jia Luo, Xi Chen, Leiming Ma,  
577 Tianning Zhang, Rui Su, et al. Fengwu: Pushing the skillful global medium-range weather forecast  
578 beyond 10 days lead. *arXiv preprint arXiv:2304.02948*, 2023a.

579

580 Kun Chen, Lei Bai, Fenghua Ling, Peng Ye, Tao Chen, Jing-Jia Luo, Hao Chen, Yi Xiao, Kang Chen,  
581 Tao Han, et al. Towards an end-to-end artificial intelligence driven global weather forecasting  
system. *arXiv preprint arXiv:2312.12462*, 2023b.

582

583 Yipeng Chen, Yishuai Jin, Zhengyu Liu, Xingchen Shen, Xianyao Chen, Xiaopei Lin, Rong-Hua  
584 Zhang, Jing-Jia Luo, Wenjun Zhang, Wansuo Duan, et al. Combined dynamical-deep learning  
585 enso forecasts. *Nature Communications*, 16(1):3845, 2025.

586

587 Yingzhe Cui, Ruohan Wu, Xiang Zhang, Ziqi Zhu, Bo Liu, Jun Shi, Junshi Chen, Hailong Liu,  
588 Shenghui Zhou, Liang Su, et al. Forecasting the eddying ocean with a deep neural network. *Nature  
Communications*, 16(1):2268, 2025.

589

590 Antoine Delaunay and Hannah M Christensen. Interpretable deep learning for probabilistic mjo  
591 prediction. *Geophysical Research Letters*, 49(16):e2022GL098566, 2022.

592

593 Ronan Fablet, Bertrand Chapron, Lucas Drumetz, Etienne Mémin, Olivier Pannekoucke, and François  
Rousseau. Learning variational data assimilation models and solvers. *Journal of Advances in  
Modeling Earth Systems*, 13(10):e2021MS002572, 2021.

- 594 Tobias Sebastian Finn, Charlotte Durand, Alban Farchi, Marc Bocquet, Pierre Rampal, and Alberto  
595 Carrassi. Generative diffusion for regional surrogate models from sea-ice simulations. Journal of  
596 Advances in Modeling Earth Systems, 16(10):e2024MS004395, 2024.
- 597  
598 Yuan Gao, Hao Wu, Ruiqi Shu, Huanshuo Dong, Fan Xu, Rui Chen, Yibo Yan, Qingsong Wen,  
599 Xuming Hu, Kun Wang, et al. Oneforecast: A universal framework for global and regional weather  
600 forecasting. arXiv preprint arXiv:2502.00338, 2025.
- 601 Joaquim Garrabou, Rafael Coma, Nathaniel Bensoussan, Marc Bally, Pierre Chevaldonné, M Cigliano,  
602 David Díaz, Jean-Georges Harmelin, María Cristina Gambi, Diego K Kersting, et al. Mass mortality  
603 in northwestern mediterranean rocky benthic communities: effects of the 2003 heat wave. Global  
604 change biology, 15(5):1090–1103, 2009.
- 605 Peter R Gent and James C McWilliams. Isopycnal mixing in ocean circulation models. Journal of  
606 Physical Oceanography, 20(1):150–155, 1990.
- 607  
608 K Giamalaki, C Beaulieu, and JX Prochaska. Assessing predictability of marine heatwaves with  
609 random forests. Geophysical Research Letters, 49(23):e2022GL099069, 2022.
- 610 Yoo-Geun Ham, Jeong-Hwan Kim, and Jing-Jia Luo. Deep learning for multi-year enso forecasts.  
611 Nature, 573(7775):568–572, 2019.
- 612  
613 Rixu Hao, Yuxin Zhao, Shaoqing Zhang, and Xiong Deng. Deep learning for ocean forecasting: A  
614 comprehensive review of methods, applications, and datasets. IEEE Transactions on Cybernetics,  
615 2025.
- 616 Sam Hatfield, Matthew Chantry, Peter Dueben, Philippe Lopez, Alan Geer, and Tim Palmer. Building  
617 tangent-linear and adjoint models for data assimilation with neural networks. Journal of Advances  
618 in Modeling Earth Systems, 13(9):e2021MS002521, 2021.
- 619  
620 Kaiming He, Xiangyu Zhang, Shaoqing Ren, and Jian Sun. Deep residual learning for image  
621 recognition. In Proceedings of the IEEE conference on computer vision and pattern recognition,  
622 pp. 770–778, 2016.
- 623 Hans Hersbach, Bill Bell, Paul Berrisford, Shoji Hirahara, András Horányi, Joaquín Muñoz-Sabater,  
624 Julien Nicolas, Carole Peubey, Raluca Radu, Dinand Schepers, et al. The era5 global reanalysis.  
625 Quarterly Journal of the Royal Meteorological Society, 146(730):1999–2049, 2020.
- 626 Alistair J Hobday, Claire M Spillman, J Paige Eveson, and Jason R Hartog. Seasonal forecasting for  
627 decision support in marine fisheries and aquaculture. Fisheries Oceanography, 25:45–56, 2016.
- 628  
629 Neil J Holbrook, Hillary A Scannell, Alexander Sen Gupta, Jessica A Benthuyssen, Ming Feng,  
630 Eric CJ Oliver, Lisa V Alexander, Michael T Burrows, Markus G Donat, Alistair J Hobday, et al.  
631 A global assessment of marine heatwaves and their drivers. Nature communications, 10(1):2624,  
632 2019.
- 633 Langwen Huang, Lukas Gianinazzi, Yuejiang Yu, Peter D Dueben, and Torsten Hoefler. Diffda: a  
634 diffusion model for weather-scale data assimilation. arXiv preprint arXiv:2401.05932, 2024.
- 635  
636 Terry P Hughes, James T Kerry, Mariana Álvarez-Noriega, Jorge G Álvarez-Romero, Kristen D  
637 Anderson, Andrew H Baird, Russell C Babcock, Maria Beger, David R Bellwood, Ray Berkelmans,  
638 et al. Global warming and recurrent mass bleaching of corals. Nature, 543(7645):373–377, 2017.
- 639 Terry P Hughes, Kristen D Anderson, Sean R Connolly, Scott F Heron, James T Kerry, Janice M  
640 Lough, Andrew H Baird, Julia K Baum, Michael L Berumen, Tom C Bridge, et al. Spatial and  
641 temporal patterns of mass bleaching of corals in the anthropocene. Science, 359(6371):80–83,  
642 2018.
- 643 Michael G Jacox, Michael A Alexander, Dillon Amaya, Emily Becker, Steven J Bograd, Stephanie  
644 Brodie, Elliott L Hazen, Mercedes Pozo Buil, and Desiree Tommasi. Global seasonal forecasts of  
645 marine heatwaves. Nature, 604(7906):486–490, 2022.
- 646  
647 Ham Kim, YG Ham, YS Joo, and SW Son. Deep learning for bias correction of mjo prediction.  
Nature Communications, 12(1):3087, 2021.

- 648 Thorsten Kurth, Shashank Subramanian, Peter Harrington, Jaideep Pathak, Morteza Mardani, David  
649 Hall, Andrea Miele, Karthik Kashinath, and Anima Anandkumar. Fourcastnet: Accelerating global  
650 high-resolution weather forecasting using adaptive fourier neural operators. In Proceedings of the  
651 platform for advanced scientific computing conference, pp. 1–11, 2023.
- 652 Stefanie Legler and Tijana Janjić. Combining data assimilation and machine learning to estimate  
653 parameters of a convective-scale model. Quarterly Journal of the Royal Meteorological Society,  
654 148(743):860–874, 2022.
- 655 Jean-Michel Lellouche, Olivier Le Galloudec, Eric Greiner, Gilles Garric, Charly Regnier, Marie  
656 Drevillon, Romain Bourdallé-Badie, Clément Bricaud, Yann Drillet, and Pierre-Yves Le Traon.  
657 The copernicus marine environment monitoring service global ocean 1/12 physical reanalysis  
658 glorys12v1: description and quality assessment. In Egu general assembly conference abstracts,  
659 pp. 19806, 2018.
- 660 Zongyi Li, Nikola Borislavov Kovachki, Kamyar Azizzadenesheli, Burigede liu, Kaushik Bhat-  
661 tacharya, Andrew Stuart, and Anima Anandkumar. Fourier neural operator for parametric partial  
662 differential equations. In ICLR, 2021.
- 663 Xingming Liang, Kevin Garrett, Quanhua Liu, Eric S Maddy, Kayo Ide, and Sid Boukabara. A deep-  
664 learning-based microwave radiative transfer emulator for data assimilation and remote sensing.  
665 IEEE Journal of Selected Topics in Applied Earth Observations and Remote Sensing, 15:8819–  
666 8833, 2022.
- 667 Zikuan Lin, Shaoqing Zhang, Zhengguang Zhang, Xiaolin Yu, and Yang Gao. The rossby normal  
668 mode as a physical linkage in a machine learning forecast model for the sst and ssh of south china  
669 sea deep basin. Journal of Geophysical Research: Oceans, 128(9):e2023JC019851, 2023.
- 670 Qi Liu and Jianwei Ma. Foundation models for geophysics: Review and perspective. arXiv preprint  
671 arXiv:2406.03163, 2024.
- 672 Ryan Wen Liu, Yuxu Lu, Yuan Gao, Yu Guo, Wenqi Ren, Fenghua Zhu, and Fei-Yue Wang. Real-time  
673 multi-scene visibility enhancement for promoting navigational safety of vessels under complex  
674 weather conditions. IEEE Transactions on Intelligent Transportation Systems, 2024.
- 675 Yang Liu, Zinan Zheng, Jiashun Cheng, Fugee Tsung, Deli Zhao, Yu Rong, and Jia Li. Cirt:  
676 Global subseasonal-to-seasonal forecasting with geometry-inspired transformer. arXiv preprint  
677 arXiv:2502.19750, 2025.
- 678 Michael J Malick, Samantha A Siedlecki, Emily L Norton, Isaac C Kaplan, Melissa A Haltuch,  
679 Mary E Hunsicker, Sandra L Parker-Stetter, Kristin N Marshall, Aaron M Berger, Albert J Hermann,  
680 et al. Environmentally driven seasonal forecasts of pacific hake distribution. Frontiers in Marine  
681 Science, 7:578490, 2020.
- 682 Boštjan Melinc and Žiga Zaplotnik. 3d-var data assimilation using a variational autoencoder.  
683 Quarterly Journal of the Royal Meteorological Society, 150(761):2273–2295, 2024.
- 684 Katherine E Mills, Andrew J Pershing, and Christina M Hernández. Forecasting the seasonal timing  
685 of maine’s lobster fishery. Frontiers in Marine Science, 4:337, 2017.
- 686 Eric CJ Oliver, Jessica A Benthuyssen, Sofia Darmaraki, Markus G Donat, Alistair J Hobday, Neil J  
687 Holbrook, Robert W Schlegel, and Alex Sen Gupta. Marine heatwaves. Annual review of marine  
688 science, 13(1):313–342, 2021.
- 689 Jaideep Pathak, Shashank Subramanian, Peter Harrington, Sanjeev Raja, Ashesh Chattopadhyay,  
690 Morteza Mardani, Thorsten Kurth, David Hall, Zongyi Li, Kamyar Azizzadenesheli, et al. Fourcast-  
691 net: A global data-driven high-resolution weather model using adaptive fourier neural operators.  
692 arXiv preprint arXiv:2202.11214, 2022.
- 693 Mark R Payne, Gokhan Danabasoglu, Noel Keenlyside, Daniela Matei, Anna K Miesner, Shuting  
694 Yang, and Stephen G Yeager. Skilful decadal-scale prediction of fish habitat and distribution shifts.  
695 Nature Communications, 13(1):2660, 2022.

- 702 Alan F Pearce, R Lenanton, G Jackson, J Moore, M Feng, and D Gaughan. The "marine heat wave"  
703 off Western Australia during the summer of 2010/11. Western Australian Fisheries and Marine  
704 Research Laboratories Hillarys, WA . . . , 2011.
- 705 William Peebles and Saining Xie. Scalable diffusion models with transformers. In Proceedings of  
706 the IEEE/CVF international conference on computer vision, pp. 4195–4205, 2023.
- 707 Marie-Isabelle Pujol, Yannice Faugère, Guillaume Taburet, Stéphanie Dupuy, Camille Pelloquin,  
708 Michael Ablain, and Nicolas Picot. Duacs dt2014: the new multi-mission altimeter data set  
709 reprocessed over 20 years. Ocean Science, 12(5):1067–1090, 2016.
- 710 Bogdan Raonic, Roberto Molinaro, Tim De Ryck, Tobias Rohner, Francesca Bartolucci, Rima  
711 Alaifari, Siddhartha Mishra, and Emmanuel de Bézenac. Convolutional neural operators for  
712 robust and accurate learning of pdes. Advances in Neural Information Processing Systems, 36:  
713 77187–77200, 2023.
- 714 Stephan Rasp, Stephan Hoyer, Alexander Merose, Ian Langmore, Peter Battaglia, Tyler Russell,  
715 Alvaro Sanchez-Gonzalez, Vivian Yang, Rob Carver, Shreya Agrawal, et al. Weatherbench 2: A  
716 benchmark for the next generation of data-driven global weather models. Journal of Advances in  
717 Modeling Earth Systems, 16(6):e2023MS004019, 2024.
- 718 Olaf Ronneberger, Philipp Fischer, and Thomas Brox. U-net: Convolutional networks for biomedical  
719 image segmentation. In Medical image computing and computer-assisted intervention–MICCAI  
720 2015: 18th international conference, Munich, Germany, October 5-9, 2015, proceedings, part III  
721 18, pp. 234–241. Springer, 2015.
- 722 Benyun Shi, Liu Feng, Hailun He, Yingjian Hao, Yue Peng, Miao Liu, Yang Liu, and Jiming Liu.  
723 A physics-guided attention-based neural network for sea surface temperature prediction. IEEE  
724 Transactions on Geoscience and Remote Sensing, 2024a.
- 725 Xingjian Shi, Zhouong Chen, Hao Wang, Dit-Yan Yeung, Wai-Kin Wong, and Wang-chun Woo.  
726 Convolutional lstm network: A machine learning approach for precipitation nowcasting. Advances  
727 in neural information processing systems, 28, 2015.
- 728 Zhensheng Shi, Haiyong Zheng, and Junyu Dong. Oceanvp: A hycom based benchmark dataset and  
729 a relational spatiotemporal predictive network for oceanic variable prediction. Ocean Engineering,  
730 304:117748, 2024b.
- 731 Na-Yeon Shin, Daehyun Kim, Daehyun Kang, Hyemi Kim, and Jong-Seong Kug. Deep learning  
732 reveals moisture as the primary predictability source of mjo. npj Climate and Atmospheric Science,  
733 7(1):11, 2024.
- 734 Ruiqi Shu, Hao Wu, Yuan Gao, Fanghua Xu, Ruijian Gou, Wei Xiong, and Xiaomeng Huang.  
735 Advanced forecasts of global extreme marine heatwaves through a physics-guided data-driven  
736 approach. Environmental Research Letters, 20(4):044030, 2025.
- 737 Patrick G Stegmann, Benjamin Johnson, Isaac Moradi, Bryan Karpowicz, and Will McCarty. A deep  
738 learning approach to fast radiative transfer. Journal of Quantitative Spectroscopy and Radiative  
739 Transfer, 280:108088, 2022.
- 740 Wenjin Sun, Shuyi Zhou, Jingsong Yang, Xiaoqian Gao, Jinlin Ji, and Changming Dong. Artificial  
741 intelligence forecasting of marine heatwaves in the south china sea using a combined u-net and  
742 convlstm system. Remote Sensing, 15(16):4068, 2023.
- 743 Cheng Tan, Zhangyang Gao, Siyuan Li, and Stan Z Li. Simvp: Towards simple yet powerful  
744 spatiotemporal predictive learning. arXiv preprint arXiv:2211.12509, 2022.
- 745 Jordan A Thomson, Derek A Burkholder, Michael R Heithaus, James W Fourqurean, Matthew W  
746 Fraser, John Statton, and Gary A Kendrick. Extreme temperatures, foundation species, and abrupt  
747 ecosystem change: an example from an iconic seagrass ecosystem. Global change biology, 21(4):  
748 1463–1474, 2015.
- 749 Yogesh Verma, Markus Heinonen, and Vikas Garg. Climode: Climate and weather forecasting with  
750 physics-informed neural odes. arXiv preprint arXiv:2404.10024, 2024.

756 Xiang Wang, Renzhi Wang, Ningzi Hu, Pinqiang Wang, Peng Huo, Guihua Wang, Huizan Wang,  
757 Sengzhang Wang, Junxing Zhu, Jianbo Xu, et al. Xihe: A data-driven model for global ocean  
758 eddy-resolving forecasting. arXiv preprint arXiv:2402.02995, 2024.

759  
760 Haixu Wu, Tengge Hu, Huakun Luo, Jianmin Wang, and Mingsheng Long. Solving high-dimensional  
761 pdes with latent spectral models. arXiv preprint arXiv:2301.12664, 2023.

762 Hao Wu, Kangyu Weng, Shuyi Zhou, Xiaomeng Huang, and Wei Xiong. Neural manifold operators  
763 for learning the evolution of physical dynamics. In Proceedings of the 30th ACM SIGKDD  
764 Conference on Knowledge Discovery and Data Mining, pp. 3356–3366, 2024a.

765  
766 Hao Wu, Fan Xu, Chong Chen, Xian-Sheng Hua, Xiao Luo, and Haixin Wang. Pastnet: Introducing  
767 physical inductive biases for spatio-temporal video prediction. In Proceedings of the 32nd ACM  
768 International Conference on Multimedia, pp. 2917–2926, 2024b.

769 Yi Xiao, Lei Bai, Wei Xue, Hao Chen, Kun Chen, Tao Han, Wanli Ouyang, et al. Towards a  
770 self-contained data-driven global weather forecasting framework. In Forty-first International  
771 Conference on Machine Learning, 2024.

772  
773 Wei Xiong, Yanfei Xiang, Hao Wu, Shuyi Zhou, Yuze Sun, Muyuan Ma, and Xiaomeng Huang.  
774 Ai-goms: Large ai-driven global ocean modeling system. arXiv preprint arXiv:2308.03152, 2023.

775 Haiqing Yu, Hui Wang, Chunxin Yuan, and Qinwang Xing. Assessing the predictability of the marine  
776 heatwave in the yellow sea during the summer of 2018 based on a deterministic forecast model.  
777 Weather and Climate Extremes, 44:100663, 2024.

778  
779  
780  
781  
782  
783  
784  
785  
786  
787  
788  
789  
790  
791  
792  
793  
794  
795  
796  
797  
798  
799  
800  
801  
802  
803  
804  
805  
806  
807  
808  
809

## A ALGORITHM

We summarize the overall framework of Ocean-E2E in Algorithm 1.

---

### Algorithm 1 Ocean-E2E Framework for Global MHWs Forecast

---

**Require:** Initial SSTA observation  $C_t^{obs}$ , analysis field  $C_{t-1}^a$  (at time  $t - 1$ ), current state of atmospheric forcing  $\mathbf{A}_t$  and ocean current velocity  $\mathbf{O}_t$ .

**Ensure:** Current step SSTA analysis field  $C_t^a$ , Next step SSTA prediction  $C_{t+1}$ .

- 1: Initialize Ocean-E2E
  - 2: **repeat**
  - 3:   **Data Assimilation**
  - 4:   Perturb the initial SSTA field  $C_{t-1}^a$  with  $N = 10$  Perlin noise  $C_{t-1}^{a(i)} = C_{t-1}^a + \varepsilon^{(i)}$ ,  $i = 1, 2, \dots, N$ .
  - 5:   Feeding the perturbed ensembles into our trained forecast model to generate forecast ensemble:  $C_t^{bg(i)} = \phi_\theta^f(C_{t-1}^{a(i)}, \mathbf{A}_{t-1:t})$ , which are also called background fields at time  $t$ .
  - 6:   Using the neural assimilation network  $\phi_\theta^a$  to produce the analysis field at time  $t$ :  $C_t^a = \phi_\theta^a(C_t^{bg(i)}, C_t^{obs})$
  - 7:   **Hybrid physics data-driven forecast**
  - 8:   Calculate the future atmospheric forcing and ocean current velocity:  $\mathbf{A}_{t+1} = \mathcal{N}_\theta(\mathbf{A}_t)$ ,  $\mathbf{O}_{t+1} = \mathcal{M}_\theta(\mathbf{O}_t)$ .
  - 9:   Taking the current analysis field  $C_t^a$ , and integrating the equation (17) with  $\mathbf{A}_{t:t+1}$  and  $\mathbf{O}_{t:t+1}$  to get the forecast field  $C_{t+1}$
  - 10: **until** converged
  - 11: **return**  $Ocean - E2E$
- 

## B DATA DETAILS

### B.1 DATASET

In this section, we will introduce the dataset used in this study in detail.

**Data used to train  $\mathcal{N}_\theta$ .** As mentioned in Section 3.2, we need to pretrain an neural network  $\mathcal{N}_\theta$  to model the evolution of the atmosphere forcing  $\mathbf{A}$ . In this study, we utilize one of the state-of-the-art weather forecast model: OneForecast Gao et al. (2025). The data used to train OneForecast is obtained from weatherbench2 Rasp et al. (2024) benchmark, which is a subset of ERA5 reanalysis data Hersbach et al. (2020). Details can be found in Table 4.

Table 4: The data used to train  $\mathcal{N}_\theta$ .

VARIABLE NAME	LAYERS	SPATIAL RESOLUTION	DT	LAT-LON RANGE	TIME
GEOPOTENTIAL (Z)	13	1.5°	6H	GLOBAL	1959~2021
SPECIFIC HUMIDITY (Q)	13	1.5°	6H	GLOBAL	1959~2021
TEMPERATURE (T)	13	1.5°	6H	GLOBAL	1959~2020
U COMPONENT OF WIND (U)	13	1.5°	6H	GLOBAL	1959~2021
V COMPONENT OF WIND (V)	13	1.5°	6H	GLOBAL	1959~2021
10 METRE U WIND COMPONENT (U10M)	1	1.5°	6H	GLOBAL	1959~2021
10 METRE V WIND COMPONENT (V10M)	1	1.5°	6H	GLOBAL	1959~2021
2 METRE TEMPERATURE (T2M)	1	1.5°	6H	GLOBAL	1959~2021
MEAN SEA LEVEL PRESSURE (MSLP)	1	1.5°	6H	GLOBAL	1959~2021

**Data used to train  $\mathcal{M}_\theta$ .** As shown in Section 3.1, like the atmosphere forcing  $\mathbf{A}$ , we need another neural network  $\mathcal{M}_\theta$  to model the ocean surface current dynamics. The data of surface current is obtained from satellite observation, which can be downloaded from [https://data.marine.copernicus.eu/product/SEALEVEL\\_GLO\\_PHY\\_L4\\_MY\\_008\\_047](https://data.marine.copernicus.eu/product/SEALEVEL_GLO_PHY_L4_MY_008_047). Details of this dataset can be found in Table 5.

Table 5: The data used to train  $\mathcal{M}_\theta$ .

VARIABLE NAME	SPATIAL RESOLUTION	DT	LAT-LON RANGE	TIME
EASTWARD SURFACE GEOSTROPHIC CURRENT VELOCITY ( $U_g$ )	0.25°	24H	GLOBAL	1993~2021
NORTHWARD SURFACE GEOSTROPHIC CURRENT VELOCITY ( $V_g$ )	0.25°	24H	GLOBAL	1993~2021

**Data used to train the hybrid data-driven network.** The training of  $\dot{S}_\theta$  and  $\mathbf{u}_\theta$  involves three atmosphere variables and three ocean variables, which can be found in Table 6. The SST dataset is selected from GLORYS12V1, which can be downloaded from [https://data.marine.copernicus.eu/product/GLOBAL\\_MULTIYEAR\\_PHY\\_001\\_030](https://data.marine.copernicus.eu/product/GLOBAL_MULTIYEAR_PHY_001_030). For regional high-resolution simulation, we choose a regional subset of GLORYS12V1 (Table 7).

Table 6: The data used to train  $\dot{S}_\theta$  and  $\mathbf{u}_\theta$  (global simulation).

VARIABLE NAME	SPATIAL RESOLUTION	DT	LAT-LON RANGE	TIME
10 METRE U WIND COMPONENT (U10M)	0.25°	24H	GLOBAL	1993~2021
10 METRE V WIND COMPONENT (V10M)	0.25°	24H	GLOBAL	1993~2021
2 METRE TEMPERATURE (T2M)	0.25°	24H	GLOBAL	1993~2021
EASTWARD SURFACE GEOSTROPHIC CURRENT VELOCITY ( $U_g$ )	0.25°	24H	GLOBAL	1993~2021
NORTHWARD SURFACE GEOSTROPHIC CURRENT VELOCITY ( $V_g$ )	0.25°	24H	GLOBAL	1993~2021
SEA SURFACE TEMPERATURE (SST)	1/12°	24H	GLOBAL	1993~2021

Table 7: The data used to train  $\dot{S}_\theta$  and  $\mathbf{u}_\theta$  (regional simulation).

VARIABLE NAME	SPATIAL RESOLUTION	DT	LAT-LON RANGE	TIME
U10M	0.25°	24H	20° ~ 60°N, 30° ~ 80°W	1993~2021
V10M	0.25°	24H	20° ~ 60°N, 30° ~ 80°W	1993~2021
T2M	0.25°	24H	20° ~ 60°N, 30° ~ 80°W	1993~2021
$U_g$	1/12°	24H	20° ~ 60°N, 30° ~ 80°W	1993~2021
$V_g$	1/12°	24H	20° ~ 60°N, 30° ~ 80°W	1993~2021
SST	1/12°	24H	20° ~ 60°N, 30° ~ 80°W	1993~2021

**Observational data.** For observational data, we utilize the Hadley Centre Integrated Ocean Database (sparse observations) and Global Ocean ODYSSEA L4 Sea Surface Temperature (satellite observations), which can be downloaded from <https://climatedataguide.ucar.edu/climate-data/hadiod-met-office-hadley-centre-integrated-ocean-database> and [https://data.marine.copernicus.eu/product/SST\\_GLO\\_PHY\\_L4\\_MY\\_010\\_044](https://data.marine.copernicus.eu/product/SST_GLO_PHY_L4_MY_010_044), respectively.

## B.2 DATA PREPROCESSING: DATA NORMALIZATION

Given that this study takes into account the primitive equations of the ocean, to avoid disrupting physical laws through normalization, we do not apply normalization to any ocean variables (including SSTA,  $U_g$ ,  $V_g$ ) in this research. Instead, normalization is only applied to atmospheric variables (including U10M, V10M, T2M).

Significant magnitude disparities exist among different atmospheric variables. To prioritize predictive capability over inter-variable magnitude differences, we implemented standardized preprocessing through normalization. Statistical parameters (mean value  $\mu$  and standard deviation  $\sigma$ ) were derived from the 1991-2018 training period, with each climate variable being assigned independent scaling

coefficients. To be specific, the normalization procedure applied the transformation:  $\mathbf{X}' = (\mathbf{X} - \mu)/\sigma$ , where  $\mathbf{X}$  denotes the raw input data.

### B.3 DATA PREPROCESSING: RESOLUTION ALIGNMENT

Since this study utilizes data from multiple sources with varying resolutions, alignment is required in both temporal and spatial dimensions. For temporal resolution, we directly combine daily averages and daily snapshots at the daily scale without special processing. For spatial resolution, we use bilinear interpolation (specifically, the `torch.nn.functional.interpolate` function) to interpolate data with different resolutions onto a unified grid of 1/2-degree (for global simulation) or 1/12-degree (for regional simulation). Additionally, for the sparse global in-situ observation data, we first filter out all sea surface observations and construct a 1/2-degree global grid. For each observation point, all corresponding grid cells within a  $1.5^\circ \times 1.5^\circ$  area centered on the observation point are assigned the respective observation data.

## C DETAILS OF DYNAMICAL CORE OF OCEAN-E2E

In this section, we are going to introduce the design of our hybrid physics data-driven model. As shown in Section 3.2, the evolution equation of our hybrid physics data-driven framework can be written as:

$$C_t = \int_0^t -(\mathbf{u}_g(t) + \mathbf{u}_\theta(\mathbf{u}_g(t), C)) \nabla C + \dot{S}_\theta(\mathbf{A}(t), C) dt + C_0 \quad (26)$$

**Spatial Discretization.** In this study, we utilized two-order center discretization to approximate  $\nabla C$ . To be sepcific,

$$\nabla C(i, j) = (\mathbf{D}_x * C(i, j), \mathbf{D}_y * C(i, j)) \quad (27)$$

Where and  $*$  is convolution operator,  $\mathbf{D}_x$  and  $\mathbf{D}_y$  are horizontal gradients, which has the form

$$\mathbf{D}_x = \begin{pmatrix} 0 & 0 & 0 \\ -1/d_{i,j} & 0 & 1/d_{i,j} \\ 0 & 0 & 0 \end{pmatrix}, \mathbf{D}_y = \begin{pmatrix} 0 & 1/s_{i,j} & 0 \\ 0 & 0 & 0 \\ 0 & -1/s_{i,j} & 0 \end{pmatrix}, \quad (28)$$

$d_{i,j}$  and  $s_{i,j}$  are longitudinal and latitudinal grid scale at  $(i, j)$ .

What's more, unlike atmosphere variables, the ocean MHWs have coastline boundary, which should be treated properly to avoid any numerical instability. In our study, we mitigate this boundary effect through a boundary mask  $\mathbf{M}$ , where

$$\mathbf{M}(i, j) = \begin{cases} 0, & \text{if the grid cell is situated on land,} \\ & \text{or if any of its neighboring cells are on land} \\ 1, & \text{else} \end{cases} \quad (29)$$

Furthermore, a scaling factor  $\varepsilon_{gm} = 0.1$  is employed on  $\mathbf{u}_{gm}$  to avoid the instability of training. The equation 26 then becomes

$$C_t = \int_0^t [ -(\mathbf{u}_g(t) + \varepsilon_{gm} \mathbf{u}_\theta(\mathbf{u}_g(t), C)) \nabla C ] \mathbf{M} + \dot{S}_\theta(\mathbf{A}(t), C) dt + C_0 \quad (30)$$

**Time Integration.** In this study, we employ the forward Euler method to approximate the time integration of the system, as described by the following discrete updates:

$$C_{(i+1)\Delta t} = C_{i\Delta t} + \left[ -(\mathbf{u}_{i\Delta t} + \mathbf{u}_\theta(\mathbf{u}_{i\Delta t}, C_{i\Delta t})) \nabla C_{i\Delta t} + \dot{S}_\theta(\mathbf{A}_{i\Delta t}, \mathbf{A}_{(i+1)\Delta t}, C_{i\Delta t}) \right] \Delta t, \quad (31)$$

$$\mathbf{u}_{(i+1)\Delta t} = \mathbf{u}_{i\Delta t} + \mathcal{M}_\theta(\mathbf{u}_{i\Delta t}) \Delta t, \quad (32)$$

$$\mathbf{A}_{(i+1)\Delta t} = \mathbf{A}_{i\Delta t} + \mathcal{N}_\theta(\mathbf{A}_{i\Delta t}) \Delta t. \quad (33)$$

For global low-resolution simulations at  $1/2^\circ$  grid spacing, we set the time step  $\Delta t = 24$  hours and integrate over a total period of  $t = 4$  days, resulting in 4 discrete steps. This coarser temporal discretization is sufficient given the relatively slower dynamics captured at this scale.

In contrast, for regional high-resolution simulations at  $1/12^\circ$  grid spacing, the rapid evolution of oceanic processes—such as mesoscale eddies and submesoscale fronts—necessitates a finer time step to maintain numerical stability and accuracy. Accordingly, we adopt  $\Delta t = 1800$  seconds (0.5 hours) and integrate over the same total period of  $t = 4$  days, amounting to 192 small steps. However, to balance computational efficiency with fidelity, the neural network corrections  $\mathbf{u}_\theta$  and  $\dot{S}_\theta$  are applied only every 48 small steps (corresponding to one day).

This hybrid approach is formalized as follows: for each daily interval indexed by  $k = 0, 1, 2, 3$  (spanning the 4-day period), we perform 48 sub-steps indexed by  $j = 0, \dots, 47$ , with the full updates applied at the end of each daily block. For  $j = 0$  to 47:

$$C_{(k \cdot 48 + j + 1)\Delta t} = C_{(k \cdot 48 + j)\Delta t} + \left[ -\mathbf{u}_{(k \cdot 48 + j)\Delta t} \nabla C_{(k \cdot 48 + j)\Delta t} \right] \Delta t. \quad (34)$$

Then, at the end of the daily block:

$$\mathbf{u}_{(k \cdot 48 + 48)\Delta t} \leftarrow \mathbf{u}_{(k \cdot 48 + 48)\Delta t} + \mathbf{u}_\theta(\mathbf{u}_{(k \cdot 48 + 48)\Delta t}, C_{(k \cdot 48 + 48)\Delta t}) \quad (35)$$

$$C_{(k \cdot 48 + 48)\Delta t} \leftarrow C_{(k \cdot 48 + 48)\Delta t} + \dot{S}_\theta \quad (36)$$

This design ensures that the computationally intensive neural network evaluations are invoked daily, while the advection term is resolved at high temporal frequency to capture fast-changing dynamics.

Furthermore, as stated in the main text, our lightweight dynamical kernel imposes no substantial computational overhead on the simulations. As demonstrated in Table 8, in regional high-resolution simulations, incorporating the dynamical core results in only a 14% increase in inference time for the Ocean-E2E model.

Table 8: Inference time for Ocean-E2E 30-day forecast (batch size=1, on a single NVIDIA RTX 3090 GPU).

Model Variant	Inference Time (ms)
Ocean-E2E w/ Dynamical Kernel	195.29
Ocean-E2E w/o Dynamical Kernel	171.58

## D DETAILS OF OUR NEURAL NETWORKS

### D.1 MULTI-SCALE CONVOLUTION

Inspired by Wu et al. (2024b), this section details the architectures of the neural network modules  $\mathcal{M}_\theta$  (for modelling ocean surface geostrophic velocity). As shown in Figure 4, both modules leverage the GABlock (Group Attention Block) as their core building unit, designed to efficiently capture multi-scale spatio-temporal features.

The foundational GABlock (specifically, a GASubBlock) processes an input feature  $\mathbf{X} \in \mathbb{R}^{B \times C_{in} \times H \times W}$ . Initially,  $\mathbf{X}$  is normalized to  $\mathbf{X}_{\text{norm1}} = \text{BN}(\mathbf{X})$ . This normalized feature is then passed through a Spatial Attention (SA) module. The SA module comprises an initial  $1 \times 1$  convolutional projection  $\mathcal{P}_1$ , an activation function  $\sigma_{\text{act}}$  (e.g., GELU), a Spatial Gating Unit (SGU), and a final  $1 \times 1$  convolutional projection  $\mathcal{P}_2$ . The core SGU employs depth-wise convolutions (DWConv<sub>0</sub>) and depth-wise dilated convolutions (DWDConv<sub>spatial</sub>). Its output is formed by a feature transformation followed by a gating mechanism:

$$\mathbf{F}_g = \text{Conv}_{1 \times 1}(\text{DWDConv}_{\text{spatial}}(\text{DWConv}_0(\sigma_{\text{act}}(\mathcal{P}_1(\mathbf{X}_{\text{norm1}})))))) \quad (37)$$

$$\mathbf{F}_x, \mathbf{G}_x = \text{split}(\mathbf{F}_g, \text{dim} = 1) \quad (38)$$

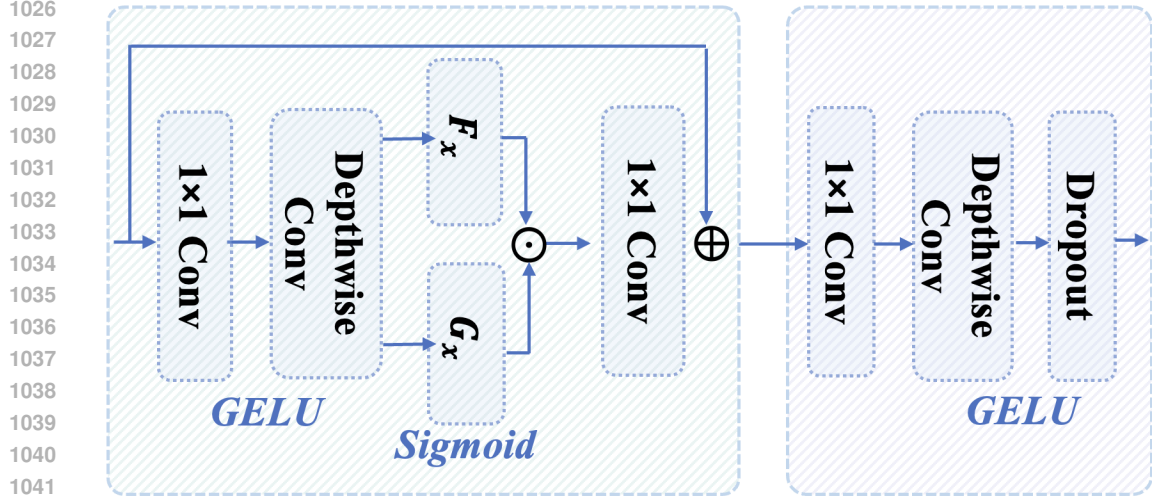


Figure 4: **Core components of the GABlock.** (Top) Core computational flow of the Multilayer Perceptron (Mlp) module, including a 1x1 convolution, a depthwise convolution, GELU activation, and Dropout. (Bottom) Core computational flow of the Spatial Attention (SA) module, illustrating the generation of feature  $F_x$  and gating signal  $G_x$  through an initial 1x1 convolution, GELU activation, and a depthwise convolution. The gating signal  $G_x$  is then passed through a Sigmoid activation and element-wise multiplied with  $F_x$ . The result is processed by a final 1x1 convolution and integrated with the input via a residual connection. These two components collectively form the key information processing units within the GABlock.

$$\text{SGU}_{\text{out}} = \sigma_{\text{sigmoid}}(\mathbf{G}_x) \odot \mathbf{F}_x \quad (39)$$

The result from the SA module,  $\mathcal{P}_2(\text{SGU}_{\text{out}})$ , is integrated back into the input via a residual connection, scaled by a learnable parameter  $\lambda_1$ :  $\mathbf{X}_{\text{attn}} = \mathbf{X} + \lambda_1 \cdot \text{DropPath}(\mathcal{P}_2(\text{SGU}_{\text{out}}))$ . Subsequently,  $\mathbf{X}_{\text{attn}}$  undergoes another normalization to  $\mathbf{X}_{\text{norm2}} = \text{BN}(\mathbf{X}_{\text{attn}})$  and is processed by a Multilayer Perceptron (MLP) module. The MLP typically consists of two 1x1 convolutions sandwiching a depth-wise convolution, along with activations and dropout. Its output,  $\text{Mlp}(\mathbf{X}_{\text{norm2}})$ , is also added residually with a learnable scale  $\lambda_2$ :  $\mathbf{X}_{\text{out}} = \mathbf{X}_{\text{attn}} + \lambda_2 \cdot \text{DropPath}(\text{Mlp}(\mathbf{X}_{\text{norm2}}))$ .

The module for approximating the geostrophic velocity,  $\mathbf{u}_g$ , adopts a U-Net-like encoder-decoder architecture. It takes the initial conditions of geostrophic currents  $\mathbf{u}_g \in \mathbb{R}^{B \times 2 \times H \times W}$  as input. The encoder path, composed of  $L_e$  stages, utilizes downsampling convolutions (e.g.,  $\text{ConvSC}$ ) and GABlocks to extract multi-scale features, denoted as  $\mathcal{H}_l$  for the  $l$ -th stage. Deeper encoder layers, particularly the bottleneck which processes  $\mathcal{H}_{L_e}$  with stacked GABlocks, are crucial for capturing non-local spatial dependencies inherent in subgrid effects. The decoder path, with  $L_d$  stages, symmetrically reconstructs spatial resolution using upsampling convolutions and GABlocks, integrating features from corresponding encoder stages  $\mathcal{H}_{L_e-l+1}$  via skip connections. A final convolutional layer then maps the decoder’s output to the future geostrophic velocity field  $\mathbf{u}_g \in \mathbb{R}^{B \times 2 \times H \times W}$ .

## D.2 NEURAL DATA ASSIMILATION NETWORK

Inspired by Liu et al. (2024), we apply an edge-reparameterization and attention-guided network to project the observation to analysis data, which achieves efficient assimilation for real-time application. It primarily consists of four parts, i.e., a convolutional layer (ConvL), a Kirsch-guided reparameterization module (KRM), a channel attention module (CAM), and a spatial attention module (SAM).

### D.2.1 CONVOLUTIONAL LAYER

The convolutional layer (ConvL) can be defined as:

$$\text{ConvL}(x_{in}) = \text{PR}(\mathcal{LN}(\text{Conv}(x_{in}))), \quad (40)$$

where  $x_{in} \in \mathbb{R}^{C \times H \times W}$  is the input of ConvL. Conv,  $\mathcal{LN}$ , and  $\mathcal{PR}$  represent the convolution operation, the layer normalization, and parametric rectified linear unit (PReLU), respectively.

## D.2.2 ATTENTION MECHANISM

The attention mechanism can realize the efficient allocation of information processing resources and can give more attention to key area of observatiou while temporarily ignoring the missing locations. Therefore, the attention mechanism is used to focus on important information with high weights, ignore irrelevant information with low weights, and continuously adjust the weights during the network learning process. Therefore, a single model can extract more valuable feature information in different imaging environments. In this work, both channel attention and spatial attention are jointly exploited to further improve the assimilation performance.

**Channel Attention Module.** The channel attention mechanism is thus exploited to reconstruct the relationship between target analysis features and the input of different observation fields. The channel attention module (CAM) can be defined as:

$$\text{CAM} = \sigma(\text{MLP}(\text{Avg}(x_{in}^c)) + \text{MLP}(\text{Max}(x_{in}^c))), \quad (41)$$

where  $x_{in}^c$  is the input of CAM, MLP denotes the multilayer perceptron, and  $\sigma$  is the Sigmoid nonlinear activation function.

**Spatial Attention Module.** In data assimilation, the spatial attention module (SAM) is used to concentrate on crucial regions, which can be defined as:

$$\text{SAM} = \sigma(\text{Conv}^{7 \times 7}([\text{Avg}(x_{in}^s); \text{Max}(x_{in}^s)])), \quad (42)$$

where  $x_{in}^s$  is the input of SAM,  $[; ]$  is exploited to concatenate two types of pooled features.

## D.2.3 KIRSCH-GUIDED REPARAMETERIZATION MODULE

To facilitate efficient assimilation in real-world MHWs forecasting, we employ the Kirsch-guided reparameterization module (KRM) with shared parameters, as proposed by Liu et al. Liu et al. (2024). The KRM is composed of three principal elements: (1) a standard convolutional layer that captures local spatial features; (2) an expand–squeeze convolutional layer that adaptively adjusts the receptive field; and (3) a family of eight directional edge-detection operators that guide the learning and inference of the convolutional kernels. Specifically, the standard convolutional and expand–squeeze operations can be formulated as follows:

$$F_n = W_n * x_{in}^k + B_n, \quad (43)$$

$$F_{es} = W_s * (W_e * x_{in}^k + B_e) + B_s, \quad (44)$$

where  $x_{in}^k$  denotes the input of KRM.  $W_n$ ,  $W_s$ ,  $W_e$ ,  $B_n$ ,  $B_s$ ,  $B_e$  are the weights and bias of convolution operation.  $F_n$  represents the output of the normal convolutional layer.  $F_{es}$  denotes the output of the expanding-and-squeezing convolutional layer. We first reparameterize the Eqs. (43) and (44). Subsequently, we merge them into a single normal convolution with parameters  $W_{es}$  and  $B_{es}$ :

$$W_{es} = \text{perm}(W_e) * W_s, \quad (45)$$

$$B_{es} = W_s * \text{rep}(B_e) + B_s, \quad (46)$$

where  $\text{perm}(\cdot)$  denotes the permute operation which exchanges the 1st and 2nd dimensions of a tensor,  $\text{rep}(\cdot)$  denotes the spatial broadcasting operation. And the predefined eight-direction Kirsch edge filters  $K_i$  are incorporated into the reparameterization module. To memorize the edge features, the input feature  $x_{in}^k$  will first be processed by  $C \times C \times 1 \times 1$  convolution and then use a custom Kirsch filter to extract the feature map gradients in eight different directions. Therefore, the edge information in eight directions can be expressed as follows:

$$\begin{aligned} F_K^i &= (S_K^i \odot K_i) \otimes (W_i * x_{in}^k + B_i) + B_{K_i} \\ &= W_K^i \otimes (W_i * x_{in}^k + B_i) + B_{K_i}, \end{aligned} \quad (47)$$

where  $W_i$  and  $B_i$  are the weights and bias of  $1 \times 1$  convolution for branches in eight directions,  $S_K^i$  and  $B_{K_i}$  are the scaling parameters and bias with the shape of  $C \times 1 \times 1 \times 1$ ,  $\odot$  indicates the

channel-wise broadcasting multiplication. The combined edge information, extracted by the scaled Kirsch filters, is given by:

$$F_K = \sum_{i=1}^8 F_K^i. \quad (48)$$

Therefore, the final weights and bias after reparameterization can be expressed as:

$$W_{\text{rep}} = W_n + W_{es} + \sum_{i=1}^8 (\text{perm}(W_i) * W_K^i), \quad (49)$$

$$B_{\text{rep}} = B_n + B_{es} + \sum_{i=1}^8 (\text{perm}(B_i) * B_{K_i}). \quad (50)$$

Finally, the output can be obtained using a single normal convolution in the inference stage:

$$F = W_{\text{rep}} * x_{in}^k + B_{\text{rep}}. \quad (51)$$

#### D.2.4 THE ASSIMILATION NETWORK

We first define the basic block:

$$res_1 = \mathcal{PR}(\mathcal{G}(\text{Conv}(x_{in}^b))), \quad (52)$$

$$res_2 = \mathcal{PR}(\mathcal{G}(\text{Conv}(res_1))), \quad (53)$$

$$res_{\text{attention}} = \text{SAM}(\text{CAM}(res_2)), \quad (54)$$

$$res_3 = \mathcal{PR}(\mathcal{G}(\text{Conv}(res_{\text{attention}})) + x_{in}^b), \quad (55)$$

$$res_4 = \mathcal{PR}(\mathcal{G}(\text{Conv}(res_3))), \quad (56)$$

where,  $x_{in}^b$  is the input of basic block,  $\mathcal{G}$  represents GroupNorm. In summary, the basic block can be defined as:

$$res_4 = \text{Block}(x_{in}^b). \quad (57)$$

Therefore, for the observation data  $x_o$ , it can be processed to analysis data as follow:

$$y_a^1 = \text{Block}(KRM(x_o) + x_o), \quad (58)$$

$$y_a^2 = \text{Block}(KRM(y_a^1) + y_a^1), \quad (59)$$

$$y_a^3 = \text{Block}(KRM(y_a^2) + y_a^2), \quad (60)$$

$$y_a^4 = \text{Block}(KRM(y_a^3) + y_a^3), \quad (61)$$

$$y_a^5 = \text{Block}(KRM(y_a^4) + y_a^4), \quad (62)$$

$$y_a^{\text{out}} = \mathcal{C}(y_a^5), \quad (63)$$

where,  $\mathcal{C}$  denotes the final convolution operation, which maps the latent information to the analysis data.

## E EXPERIMENTS DETAILS

### E.1 EVALUATION METRIC

**Definition of MHWs.** The Hobday et al. (2016) definition of MHW categories is applied to detect MHWs from original SST field. More precisely, any interval in which the SST anomalies surpass the 90th percentile for a minimum of five days in a row is classified as an MHW event.

**Metrics.** In this study, to evaluate the performance of our model, we use three metrics: Root Mean Square Error (RMSE), Critical Success Index (CSI) and Bias (BIAS). RMSE represents the overall performance of our SST anomaly forecast, which is calculated as:

$$\text{RMSE}(t) = \sqrt{\frac{1}{H \times W} \sum_{i,j} \omega_{i,j} (C_{i,j}(t) - \tilde{C}_{i,j}(t))^2} \quad (64)$$

Where  $C_{i,j}(t)$  and  $\tilde{C}_{i,j}(t)$  is the ground truth and prediction of SST anomaly at lead time  $t$ ,  $\omega_{i,j}$  is the weighting coefficient and the subscript  $(i, j)$  indicates the data at grid point  $(i, j)$  while  $H$  and  $W$  follow the same definition in Section 2. CSI is the metric that evaluate the forecast ability of extreme events and can be expressed as:

$$\text{CSI}(t) = \frac{\text{TP}}{\text{TP} + \text{FP} + \text{FN}} \quad (65)$$

Where TP (True Positive) denotes the number of cases that a MHW event is accurately predicted. FP (False Positive), FN (False Negative), and TN (True Negative) follow a similar definition.

BIAS is used to evaluate the systematic difference between the analysis field and the ground truth:

$$\text{BIAS}(t) = \frac{1}{H \times W} \sum_{i,j} \omega_{i,j} (C_{i,j}(t) - \tilde{C}_{i,j}(t)) \quad (66)$$

## E.2 MODEL TRAINING

All baseline models and Ocean-E2E were trained under identical experimental configurations to ensure fair comparison. The training process employed 100 epochs with an initial learning rate of  $1 \times 10^{-3}$ , utilizing a step-wise learning rate scheduler to dynamically adjust training parameters until convergence was achieved. For objective evaluation, model checkpoints demonstrating optimal performance on the validation set were selected as final candidates for comparative analysis.

## F RELATED WORK AND LIMITATIONS

### F.1 NUMERICAL MODEL BASED OCEAN FORECASTING

Traditional MHWs forecasting predominantly relies on numerical models solving oceanic primitive equations. These approaches are typically categorized into two types: (1) seasonal forecasting, which predicts large-scale MHW characteristics including onset timing, duration, and intensity evolution Jacox et al. (2022); Brodie et al. (2023), and (2) sub-seasonal forecasting, which resolves finer spatiotemporal variations at the cost of reduced prediction horizons Benthuisen et al. (2021); Yu et al. (2024). While physics-based models demonstrate reasonable forecast skill, they face two principal limitations: prohibitive computational costs scaling with model resolution Xiong et al. (2023); Wang et al. (2024), and systematic underestimation of extreme MHW magnitudes Jacox et al. (2022).

### F.2 DEEP LEARNING BASED OCEAN FORECASTING

Machine learning (ML) techniques have emerged as promising alternatives for oceanic modeling, offering orders-of-magnitude speedup over conventional methods Liu & Ma (2024); Hao et al. (2025). Recent efforts have developed spatio-temporal architectures including NMO Wu et al. (2024a), neXtSIM Finn et al. (2024), and OceanVP Shi et al. (2024b) for regional ocean modeling, alongside specialized models for specific oceanic phenomena such as ENSO Ham et al. (2019); Chen et al. (2025), MJO Kim et al. (2021); Delaunay & Christensen (2022); Shin et al. (2024), and MHWs Shi et al. (2024a); Jacox et al. (2022); Shu et al. (2025). Building on advances in atmospheric foundation models Pathak et al. (2022); Bi et al. (2023), the community has recently proposed global ocean foundation models like AI-GOMS Xiong et al. (2023), Xihe Wang et al. (2024), and WenHai Cui et al. (2025).

### F.3 DEEP LEARNING BASED DATA ASSIMILATION

Deep learning (DL) has shown transformative potential in weather and climate data assimilation (DA), with progress evolving along three directions: (1) Conceptual validation using idealized systems like Lorenz models and shallow water equations Brajard et al. (2020); Arcucci et al. (2021); Fablet et al. (2021); Legler & Janjić (2022); (2) Component replacement within conventional DA frameworks, including physical parameterization Hatfield et al. (2021), observation operators Liang et al. (2022); Stegmann et al. (2022), and optimization cost functions Melinc & Zaplotnik (2024); Xiao et al. (2024); (3) End-to-end DA system replacement, exemplified by FengWu-Adas and DiffDA that

1242 implement complete DL-based assimilation pipelines using ERA5 reanalysis data Chen et al. (2023b);  
 1243 Huang et al. (2024).

#### 1244 F.4 LIMITATIONS

1245  
 1246 Despite the promising results demonstrated by our proposed Ocean-E2E framework, several limi-  
 1247 tations should be acknowledged. First, the hybrid approach relies on certain simplifications of the  
 1248 underlying physical processes, which may not fully capture the complex, multi-scale interactions in  
 1249 certain oceanic regimes. Second, the current model does not explicitly account for potential feedback  
 1250 mechanisms between marine heatwaves and larger-scale climate modes, which may affect the accu-  
 1251 racy of long-term forecasts. Future work could focus on refining the physical constraints, expanding  
 1252 the evaluation across diverse marine environments, and exploring more efficient architectures to  
 1253 enhance robustness and operational feasibility.  
 1254  
 1255

## 1256 G ADDITIONAL RESULTS

### 1257 G.1 ADDITIONAL RESULTS OF OUR END-TO-END FORECAST SYSTEM

1258  
 1259 In this section, we are going to show additional results of our end-to-end forecast system.  
 1260

1261  
 1262 **Details of the performance of our assimilation framework.** Figure 5 illustrates the performance of  
 1263 our assimilation, including a snapshot of our analysis field and temporal evolution of our assimilation  
 1264 error.  
 1265

1266 **Additional comparisons between our framework and S2S.** To be specific, we take the S2S analysis  
 1267 field as the groundtruth, and use it to initialize our Ocean-E2E. The atmospheric boundary condition  
 1268 is acquired through one of the state-of-the-art AI-driven weather forecast model: OneForecast Gao  
 1269 et al. (2025). As shown in Table 10, our model still performs better than S2S.  
 1270

1271 **Ablation Analysis on Error Propagation.** We further present the ablation results for the core  
 1272 components of the marine heatwave forecasting task to investigate how errors propagate through  
 1273 the atmospheric forcing forecast module  $\mathcal{N}_\theta$  and the assimilation module  $\phi_\theta^a$ . As shown in Table 9,  
 1274 comparing the full Ocean-E2E model with variants using real atmospheric forcing (w/o  $\mathcal{N}_\theta$ ) and real  
 1275 initial conditions (w/o  $\phi_\theta^a$ ), we observe that the error in the atmospheric forecast module accumulates  
 1276 gradually over time (e.g., the gap between w/o  $\mathcal{N}_\theta$  and Full model widens at 40-day lead time). This  
 1277 underscores the critical role of accurate atmospheric forcing fields. In contrast, the assimilation  
 1278 module does not exhibit a significant cumulative error effect, as it primarily impacts the state fields in  
 1279 the immediate vicinity of the assimilation timestamp, thereby exerting a localized effect.

1280 Table 9: Ablation study on core components regarding error propagation. We compare the RMSE of  
 1281 Global SSTA across different lead times (20 and 40 days) for the years 2020 and 2021.  
 1282

Model Variants	2020		2021	
	20-day	40-day	20-day	40-day
w/o $\mathcal{N}_\theta$ (real atmosphere)	0.5944	0.8325	0.7297	0.8132
w/o $\phi_\theta^a$ (real IC)	0.5832	0.8691	0.6965	0.8531
<b>Ocean-E2E (Full)</b>	<b>0.6047</b>	<b>0.8747</b>	<b>0.7447</b>	<b>0.8729</b>

### 1283 G.2 ADDITIONAL EVALUATIONS OF OUR MODEL’S PERFORMANCE

1284  
 1285  
 1286 In this section, we present the power spectrum of the squared modulus of the SSTA gradient,  $|\nabla C|^2$ ,  
 1287 on day 20. As shown in Figure 6, our Ocean-E2E model, especially at small scales (corresponding to  
 1288 a large wave number), is closer to the ground truth. This additional evaluation metric demonstrates  
 1289 the accuracy of our model in simulating the heatwave system.  
 1290

1296  
1297  
1298  
1299  
1300  
1301  
1302  
1303  
1304  
1305  
1306  
1307  
1308  
1309  
1310  
1311  
1312  
1313  
1314  
1315  
1316  
1317  
1318  
1319  
1320  
1321  
1322  
1323  
1324  
1325  
1326  
1327  
1328  
1329  
1330  
1331  
1332  
1333  
1334  
1335  
1336  
1337  
1338  
1339  
1340  
1341  
1342  
1343  
1344  
1345  
1346  
1347  
1348  
1349

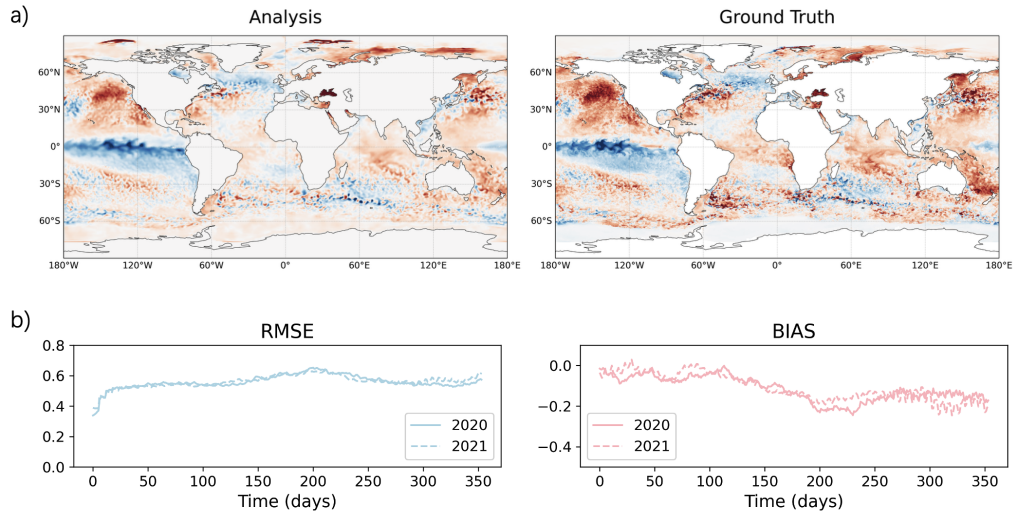


Figure 5: Results of our end-to-end assimilation framework. a) Snapshots of our analysis field and the groundtruth after 300 days of the initialization of our assimilation in 2020 b) Temporal evolution of RMSE and BIAS during the assimilation period.

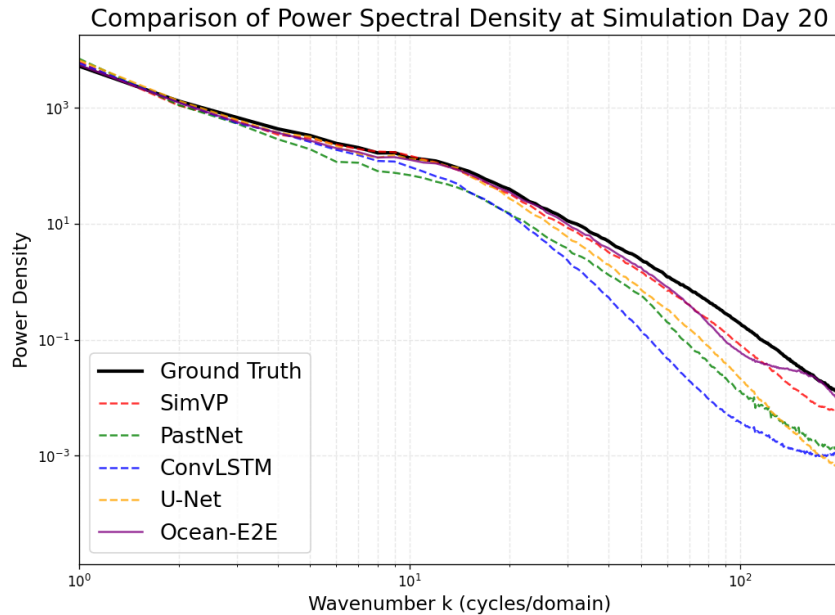


Figure 6: Power Spectrum of  $|\nabla C|^2$  on day 20 from our regional simulation experiment.

### G.3 VISUALIZATION OF GLOBAL MHWs SIMULATION

In this section, we visualize the global MHWs forecast result of our Ocean-E2E, as shown in Figure 7-9. **We plot the global SSTA field, where darkred parts indicate strong MHWs.**

### G.4 VISUALIZATION OF GLOBAL MHWs FORECAST

In this section, we visualize the global MHWs forecast result of our Ocean-E2E, as shown in Figure 10-12. **We plot the global SSTA field, where darkred parts indicate strong MHWs.**

1350 Table 10: Additional comparison with S2S. The average results for global SSTA of RMSE are  
 1351 recorded. A small RMSE ( $\downarrow$ ) indicates better performance. The best results are in **bold**, and the  
 1352 second best are with underline.

MODEL	METRIC (RMSE)			
	TIME INTERVAL			
	14-DAY	21-DAY	28-DAY	35-DAY
S2S (2020)	0.5249	0.5994	0.6618	0.7086
OCEAN-E2E (2020)	<b>0.4321</b>	<b>0.5242</b>	<b>0.5891</b>	<b>0.6304</b>
OCEAN-E2E (PROMOTION)	17.8 %	12.5 %	11.0 %	11.0 %
S2S (2021)	0.5175	0.5703	0.6121	0.6448
OCEAN-E2E (2021)	<b>0.4350</b>	<b>0.5167</b>	<b>0.5626</b>	<b>0.6022</b>
OCEAN-E2E (PROMOTION)	15.9 %	9.4 %	8.1 %	6.6 %

### 1366 G.5 VISUALIZATION OF REGIONAL HIGH RESOLUTION SIMULATION

1367 In this section, we visualize the regional (western Atlantic) simulation, as shown in Figure 13-15. **We**  
 1368 **plot the regional SSTA field, where yellow parts indicate MHWs.**

## 1371 H LARGE LANGUAGE MODEL (LLM) USE DISCLOSURE

1372 No large language models were used in the creation of this work for the purposes of writing assistance,  
 1373 literature retrieval, research ideation, or any other aspect of the research and manuscript preparation  
 1374 process.  
 1375

1376  
1377  
1378  
1379  
1380  
1381  
1382  
1383  
1384  
1385  
1386  
1387  
1388  
1389  
1390  
1391  
1392  
1393  
1394  
1395  
1396  
1397  
1398  
1399  
1400  
1401  
1402  
1403

1404  
1405  
1406  
1407  
1408  
1409  
1410  
1411  
1412  
1413  
1414  
1415  
1416  
1417  
1418  
1419  
1420  
1421  
1422  
1423  
1424  
1425  
1426  
1427  
1428  
1429  
1430  
1431  
1432  
1433  
1434  
1435  
1436  
1437  
1438  
1439  
1440  
1441  
1442  
1443  
1444  
1445  
1446  
1447  
1448  
1449  
1450  
1451  
1452  
1453  
1454  
1455  
1456  
1457

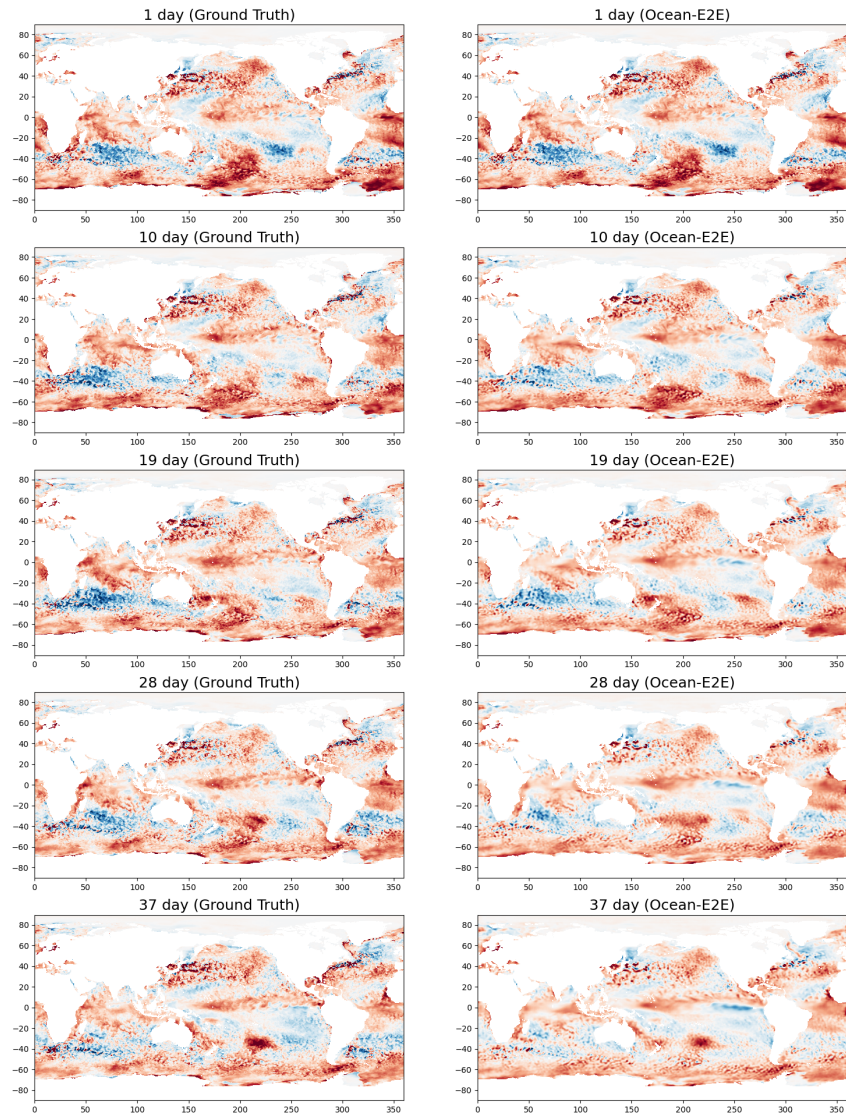


Figure 7: Global Simulation of MHWs Initialized on January 13, 2020

1458  
1459  
1460  
1461  
1462  
1463  
1464  
1465  
1466  
1467  
1468  
1469  
1470  
1471  
1472  
1473  
1474  
1475  
1476  
1477  
1478  
1479  
1480  
1481  
1482  
1483  
1484  
1485  
1486  
1487  
1488  
1489  
1490  
1491  
1492  
1493  
1494  
1495  
1496  
1497  
1498  
1499  
1500  
1501  
1502  
1503  
1504  
1505  
1506  
1507  
1508  
1509  
1510  
1511

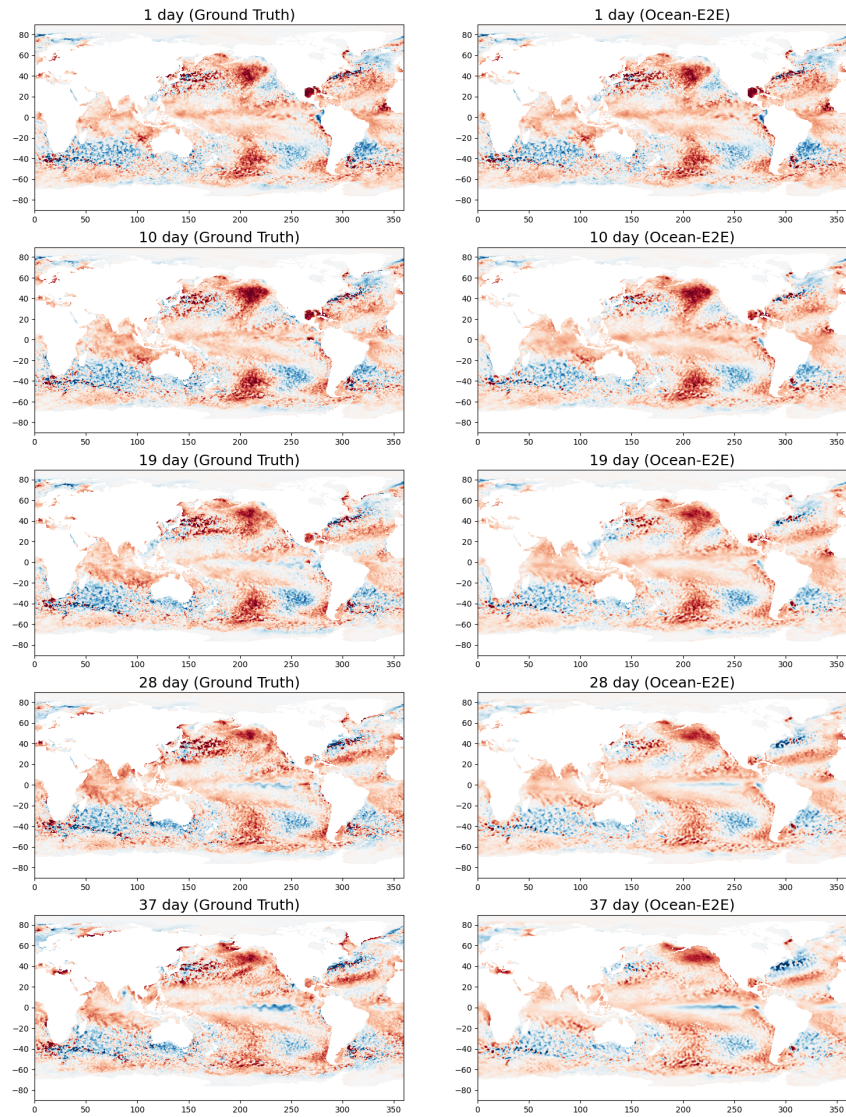


Figure 8: Global Simulation of MHWs Initialized on May 12, 2020

1512  
1513  
1514  
1515  
1516  
1517  
1518  
1519  
1520  
1521  
1522  
1523  
1524  
1525  
1526  
1527  
1528  
1529  
1530  
1531  
1532  
1533  
1534  
1535  
1536  
1537  
1538  
1539  
1540  
1541  
1542  
1543  
1544  
1545  
1546  
1547  
1548  
1549  
1550  
1551  
1552  
1553  
1554  
1555  
1556  
1557  
1558  
1559  
1560  
1561  
1562  
1563  
1564  
1565

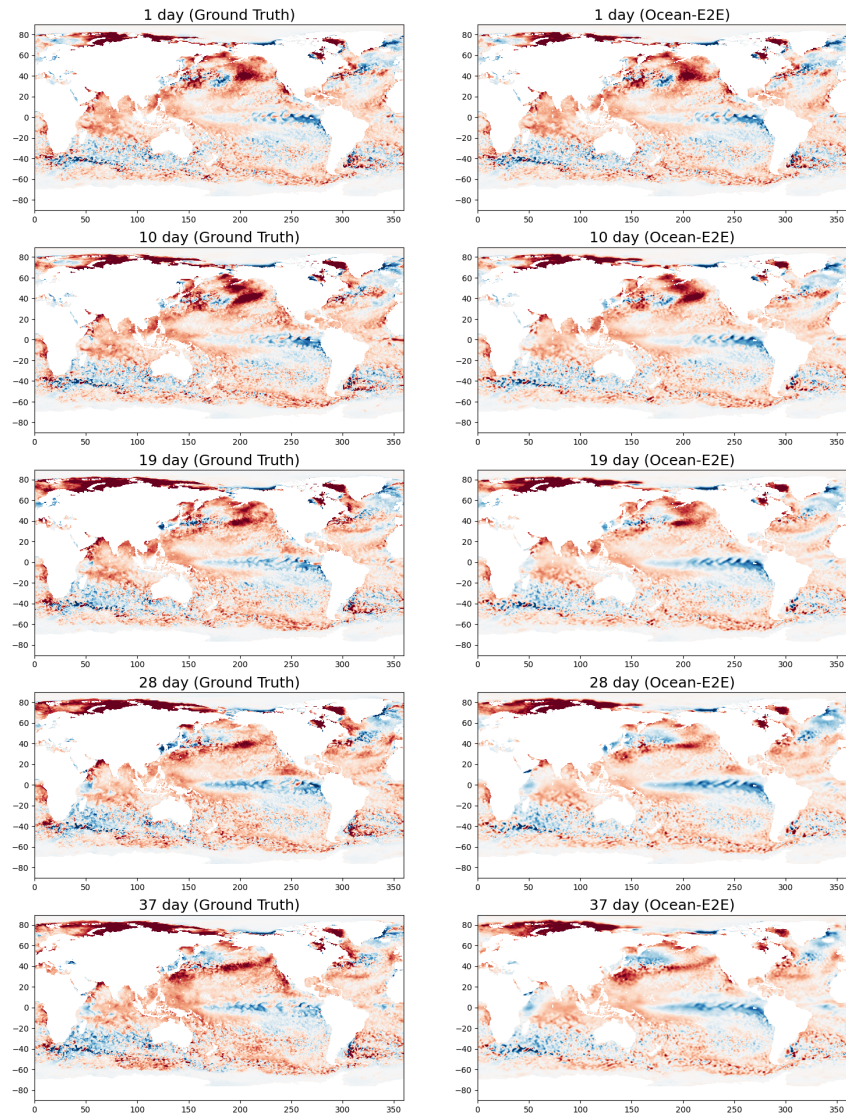


Figure 9: Global Simulation of MHWs Initialized on July 11, 2020

1566  
1567  
1568  
1569  
1570  
1571  
1572  
1573  
1574  
1575  
1576  
1577  
1578  
1579  
1580  
1581  
1582  
1583  
1584  
1585  
1586  
1587  
1588  
1589  
1590  
1591  
1592  
1593  
1594  
1595  
1596  
1597  
1598  
1599  
1600  
1601  
1602  
1603  
1604  
1605  
1606  
1607  
1608  
1609  
1610  
1611  
1612  
1613  
1614  
1615  
1616  
1617  
1618  
1619

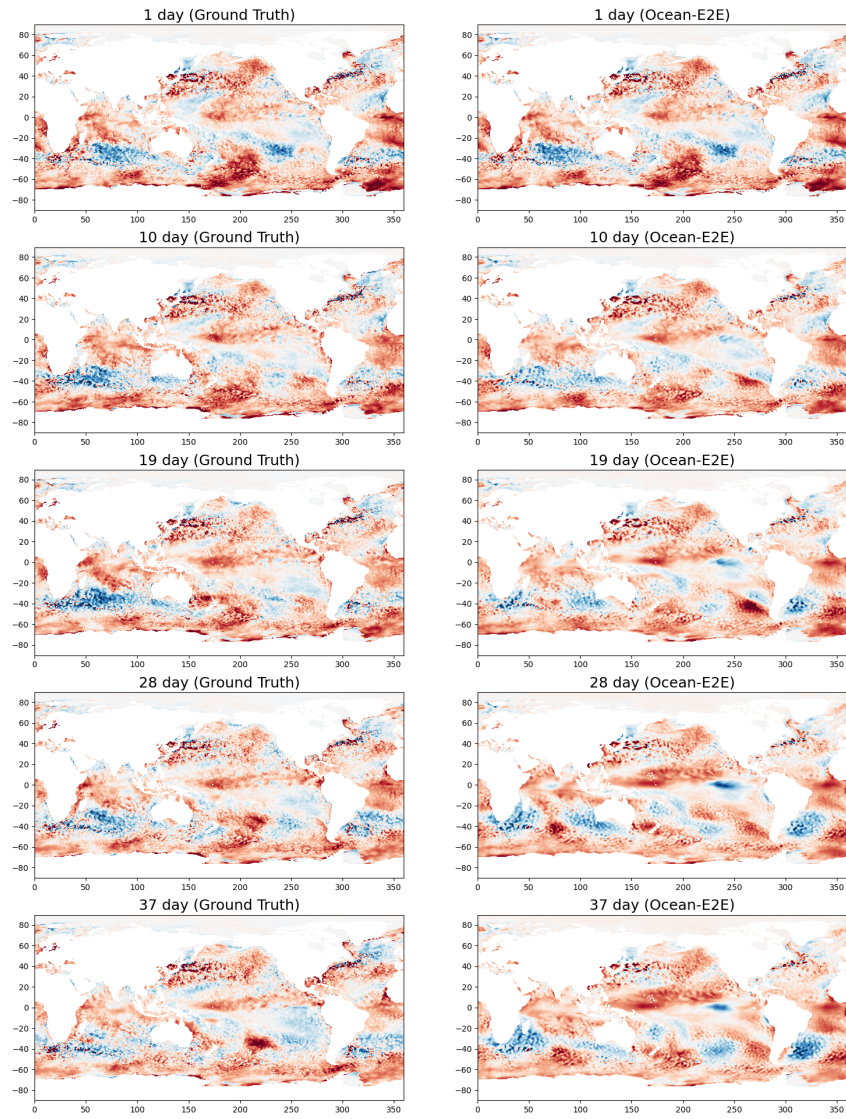


Figure 10: Global Forecast of MHWs Initialized on January 13, 2020

1620  
1621  
1622  
1623  
1624  
1625  
1626  
1627  
1628  
1629  
1630  
1631  
1632  
1633  
1634  
1635  
1636  
1637  
1638  
1639  
1640  
1641  
1642  
1643  
1644  
1645  
1646  
1647  
1648  
1649  
1650  
1651  
1652  
1653  
1654  
1655  
1656  
1657  
1658  
1659  
1660  
1661  
1662  
1663  
1664  
1665  
1666  
1667  
1668  
1669  
1670  
1671  
1672  
1673

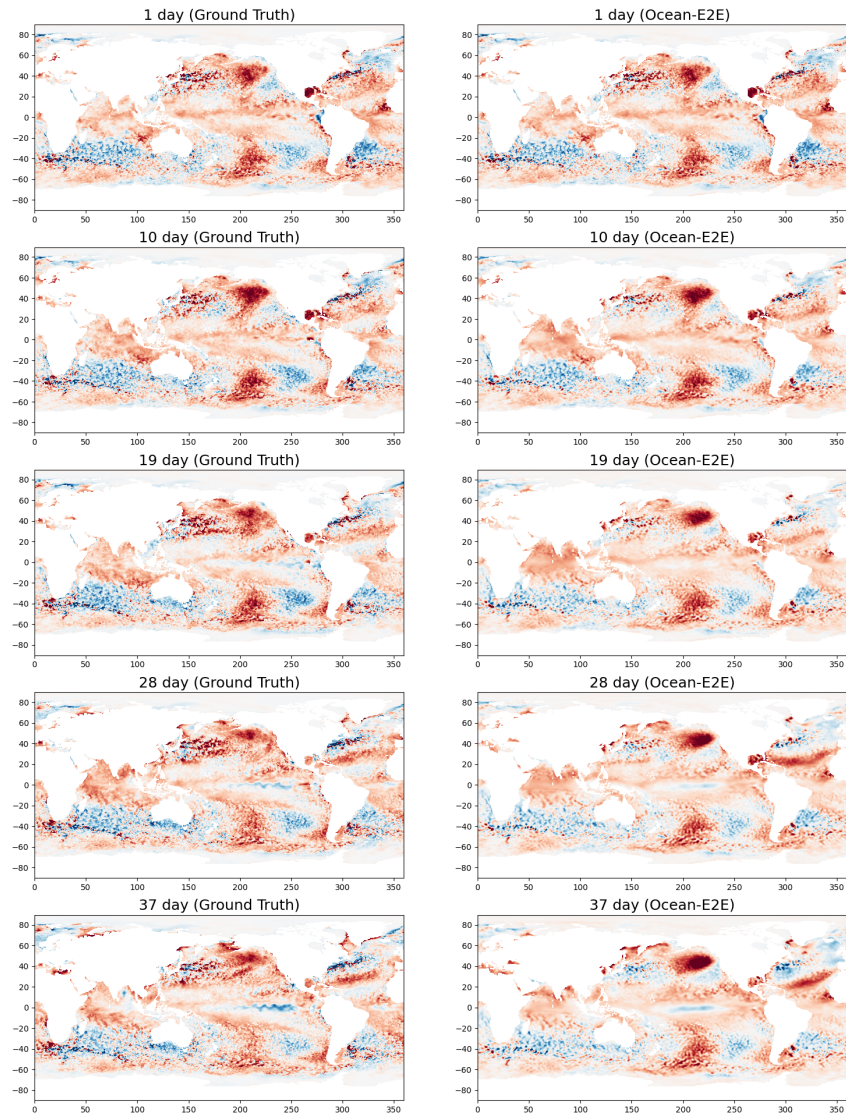


Figure 11: Global Forecast of MHWs Initialized on May 12, 2020

1674  
1675  
1676  
1677  
1678  
1679  
1680  
1681  
1682  
1683  
1684  
1685  
1686  
1687  
1688  
1689  
1690  
1691  
1692  
1693  
1694  
1695  
1696  
1697  
1698  
1699  
1700  
1701  
1702  
1703  
1704  
1705  
1706  
1707  
1708  
1709  
1710  
1711  
1712  
1713  
1714  
1715  
1716  
1717  
1718  
1719  
1720  
1721  
1722  
1723  
1724  
1725  
1726  
1727

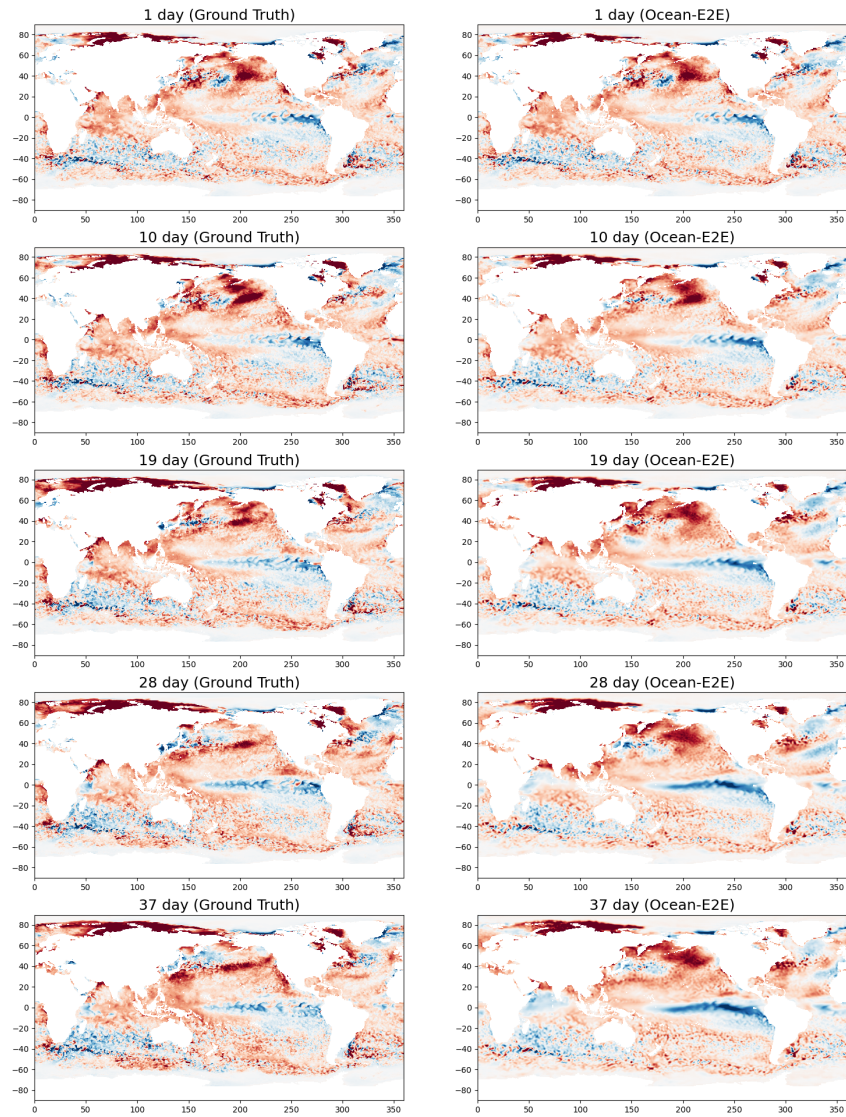


Figure 12: Global Forecast of MHWs Initialized on July 11, 2020

1728  
1729  
1730  
1731  
1732  
1733  
1734  
1735  
1736  
1737  
1738  
1739  
1740  
1741  
1742  
1743  
1744  
1745  
1746  
1747  
1748  
1749  
1750  
1751  
1752  
1753  
1754  
1755  
1756  
1757  
1758  
1759  
1760  
1761  
1762  
1763  
1764  
1765  
1766  
1767  
1768  
1769  
1770  
1771  
1772  
1773  
1774  
1775  
1776  
1777  
1778  
1779  
1780  
1781

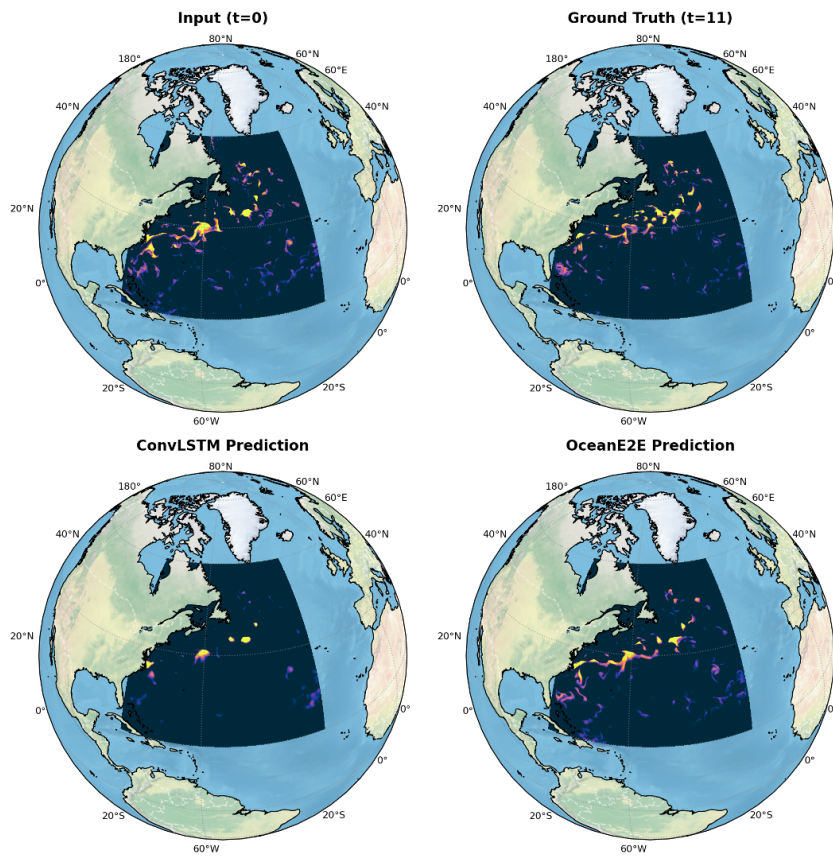


Figure 13: Regional Simulation of West Atlantic Initialized on January 13, 2020

1782  
1783  
1784  
1785  
1786  
1787  
1788  
1789  
1790  
1791  
1792  
1793  
1794  
1795  
1796  
1797  
1798  
1799  
1800  
1801  
1802  
1803  
1804  
1805  
1806  
1807  
1808  
1809  
1810  
1811  
1812  
1813  
1814  
1815  
1816  
1817  
1818  
1819  
1820  
1821  
1822  
1823  
1824  
1825  
1826  
1827  
1828  
1829  
1830  
1831  
1832  
1833  
1834  
1835

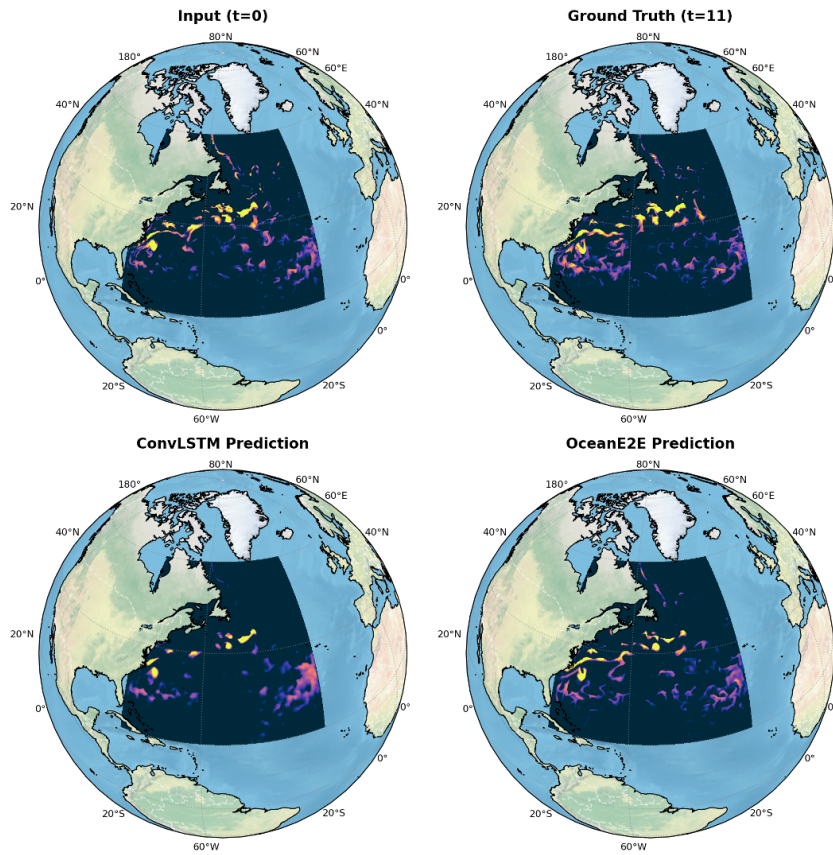


Figure 14: Regional Simulation of West Atlantic Initialized on March 13, 2020

1836  
1837  
1838  
1839  
1840  
1841  
1842  
1843  
1844  
1845  
1846  
1847  
1848  
1849  
1850  
1851  
1852  
1853  
1854  
1855  
1856  
1857  
1858  
1859  
1860  
1861  
1862  
1863  
1864  
1865  
1866  
1867  
1868  
1869  
1870  
1871  
1872  
1873  
1874  
1875  
1876  
1877  
1878  
1879  
1880  
1881  
1882  
1883  
1884  
1885  
1886  
1887  
1888  
1889

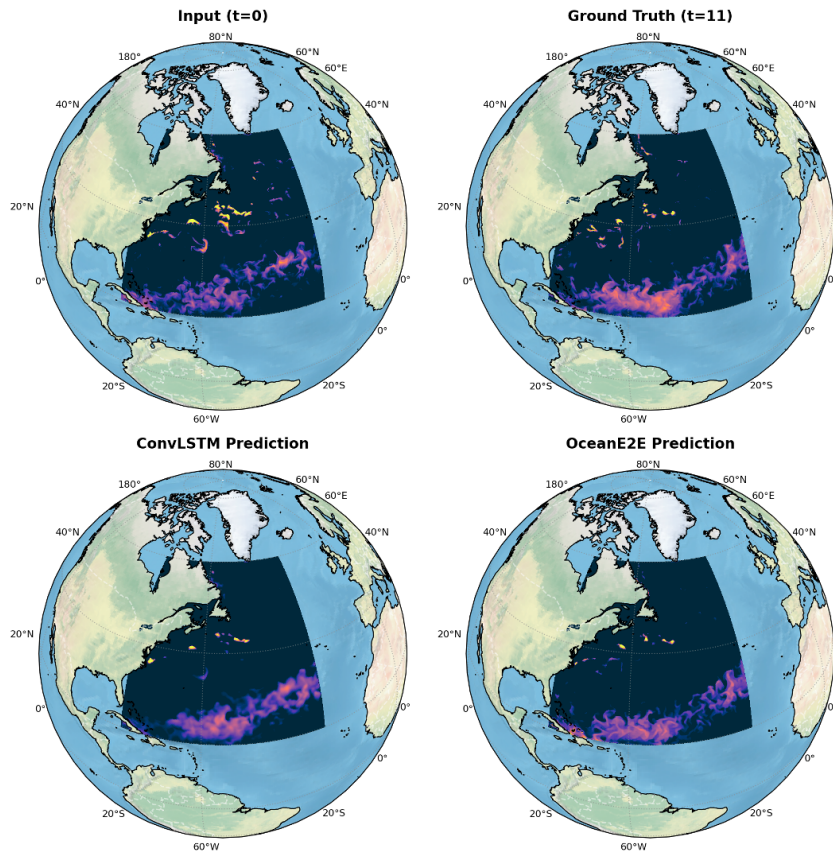


Figure 15: Regional Simulation of West Atlantic Initialized on May 12, 2020